Adsorption and reaction of methanol on supported palladium catalysts: microscopic-level studies from ultrahigh vacuum to ambient pressure conditions†

Marcus Bäumer,[a] Jörg Libuda,‡*[b] Konstantin M. Neyman,§[c] Notker Rösch,[c] Günther Rupprechter¶[b] and Hans-Joachim Freund[b]

Received 9th January 2007, Accepted 11th April 2007
First published as an Advance Article on the web 18th May 2007
DOI: 10.1039/b700365j

We investigated the decomposition and (partial) oxidation of methanol on Pd based catalysts in an integrated attempt, simultaneously bridging both the pressure and the materials gap. Combined studies were performed on well-defined Pd model catalysts based on ordered Al_2O_3 and Fe_3O_4 thin films, on well-defined particles supported on powders and on Pd single crystals. The interaction of Pd nanoparticles and Pd(111) with CH_3OH and CH_3OH/O_2 mixtures was examined from ultrahigh vacuum conditions up to ambient pressures, utilizing a broad range of surface specific vibrational spectroscopies which included IRAS, TR-IRAS, PM-IRAS, SFG, and DRIFTS. Detailed kinetic studies in the low pressure region were performed by molecular beam methods, providing comprehensive insights into the microkinetics of the reaction system. The underlying microscopic processes were studied theoretically on the basis of specially designed 3-D nanocluster models containing $\sim 10^2$ metal atoms. The efficiency of this novel modelling approach was demonstrated by rationalizing and complementing pertinent experimental results. In order to connect these results to the behavior under ambient conditions, kinetic and spectroscopic investigations were performed in reaction cells and lab reactors. Specifically, we focused on (1) particle size and structure dependent effects in methanol oxidation and decomposition, (2) support effects and their relation to activity and selectivity, (3) the influence of poisons such as carbon, and (4) the role of oxide and surface oxide formation on Pd nanoparticles.

1. Introduction: towards an understanding of heterogeneous catalysis at the microscopic level

Heterogeneous catalysis is one of the key phenomena in 21st century technology.[1,2] The production of most chemicals involves heterogeneously catalyzed steps, similarly to numerous processes in environmental technology and energy storage.

In spite of this enormous economical role, there is only little fundamental understanding of the mechanism and kinetics of the underlying chemical reactions. Such insights into catalytic processes at the molecular level could be provided by detailed surface science studies.[3,4] However, the direct transfer of scientific results from surface science to applied catalysis requires to overcome two main difficulties:

— The first challenge is related to the so-called "materials gap" (see, *e.g.*, ref. 5–7): whereas surface science studies typically focus on single crystal surfaces, heterogeneous catalysts are complex materials. Often, they are based on metal or alloy nanoparticles supported on simple or mixed porous oxides, which may be further modified by multiple poisons or promoters. It is this complexity which allows optimization of heterogeneous catalysts, taking advantage of particle size, structure or support dependent effects only in an empirical fashion. A microscopic interpretation of these effects is missing in most cases, however. One route towards a more detailed understanding and a microscopically founded microkinetic modelling involves the development of well-defined model catalysts (see *e.g.*, ref. 8–12). These model systems allow us to introduce certain complex features of real catalysts, without having to deal with the full complexity of the real system. The model systems which are in the focus of the present review are briefly described in section 4.

The second challenge is related to the so-called "pressure gap" between surface science and catalysis: Typically, surface science studies are performed under ultrahigh-vacuum (UHV) conditions, in order to avoid uncontrolled surface contamination. Furthermore, many experimental techniques such as electron spectroscopies require high vacuum conditions. Industrial catalytic reactors are typically run at ambient pressure or elevated pressures, however. It remains to be established whether the results obtained under UHV conditions can be

[a] *Institut für Angewandte und Physikalische Chemie, Universität Bremen, Leobener Str. NW2, D-28359 Bremen, Germany*
[b] *Fritz-Haber-Institut der Max-Planck-Gesellschaft, Faradayweg 4-6, D-14195 Berlin, Germany*
[c] *Department Chemie, Technische Universität München, Lichtenbergstr. 4, D-85748 Garching, Germany*
† The HTML version of this article has been enhanced with colour images.
‡ Present address: Lehrstuhl für Physikalische Chemie II, Universität Erlangen-Nürnberg, Egerlandstr. 3, D-91058 Erlangen, Germany.
§ Present address: Institució Catalana de Recerca i Estudis Avançats (ICREA), E-08010 Barcelona and Departament de Química Física, Universitat de Barcelona, E-08028 Barcelona, Spain.
¶ Present address: Institut für Materialchemie, Technische Universität Wien, Veterinärplatz 1, A-1210 Wien, Austria.

transferred to the elevated pressure regime. Linking the two worlds requires the development of spectroscopic tools which cover the full pressure range from UHV to 1 bar. Several such ''pressure gap methods'' have recently entered the field of surface science (see *e.g.* ref. 13–24). In section 3 we briefly discuss the methods that have been applied in the studies reviewed here.

2. Methanol as a model reactant in surface science and catalysis

Before discussing experimental methods and model systems in detail, a suitable target reaction has to be identified. In the series of studies reviewed here, we have chosen to focus on the reactions of methanol on different types of Pd-based model catalysts. Methanol plays an important role as an intermediate product in chemical industry, but also as a potential future energy carrier.[25–27] Synthesis of methanol is among the largest-scale industrial applications of heterogeneous catalysis, based on the so-called ICI process. The ICI catalyst contains $Cu/ZnO/Al_2O_3$ as the active phase (see, *e.g.*, ref. 28). $Pd/CaO/SiO_2$ based catalysts have shown similar performance, however.[29,30] Partial oxidation of CH_3OH to CH_2O represents a further highly relevant industrial process. For the partial and total oxidation of CH_3OH (including generation of H_2 in order to exploit CH_3OH as a hydrogen carrier), Pd based catalysts have been considered as well.[31–33]

The reaction network for methanol decomposition/oxidation is schematically summarized in Fig. 1a.[34,35] Methanol first adsorbs on the support and on the metal particles. Diffusion and spillover of molecular methanol and methoxy species may lead to an additional flux of reactants from/to the active Pd particles. Decomposition of methanol proceeds *via* formation of methoxy (CH_3O) species, followed by either C–H or C–O bond scission. C–H bond scission leads to formaldehyde (CH_2O), formyl (CHO) and finally CO, followed by oxidation to CO_2 in the presence of adsorbed oxygen. The competing route involves scission of the C–O bond, resulting in hydrocarbon entities and finally carbon species after complete dehydrogenation. O and C atomic co-adsorbates may play a critical role under reaction conditions. In the presence of oxygen, surface and bulk oxidation may occur, whereas carbon can accumulate on the surface, but also in the subsurface and bulk region. Both effects lead to changes in activity and selectivity of the catalyst.

There are several arguments, which make the oxidation/decomposition of methanol on Pd based catalysts, in spite of its apparent complexity, an ideal model system for studies on the issues of the ''pressure and materials gaps'':

(i) Selectivity in a complex reaction network

Besides mechanistic and kinetic studies, one of the greatest challenges in catalysis is related to a microscopic-level understanding of selectivity.[36] From both an experimental and theoretical points of view, this turns out to be a demanding task as selectivity is controlled by quite subtle differences in the kinetics and thermodynamics of a reaction network. Methanol oxidation/dehydrogenation provides a sufficiently complex system in order to exemplify such effects. The competition between the two reaction pathways makes the system a very attractive candidate to study the microscopic origins of selectivity changes in a combined experimental and theoretical effort (see section 5). The situation is particularly favorable as many of the elementary reactions involved, such as adsorption and desorption of CO, oxygen and hydrogen, CO oxidation, oxide formation/decomposition and carbon adsorption/incorporation could be studied separately. These different pieces of information may finally be combined in order to

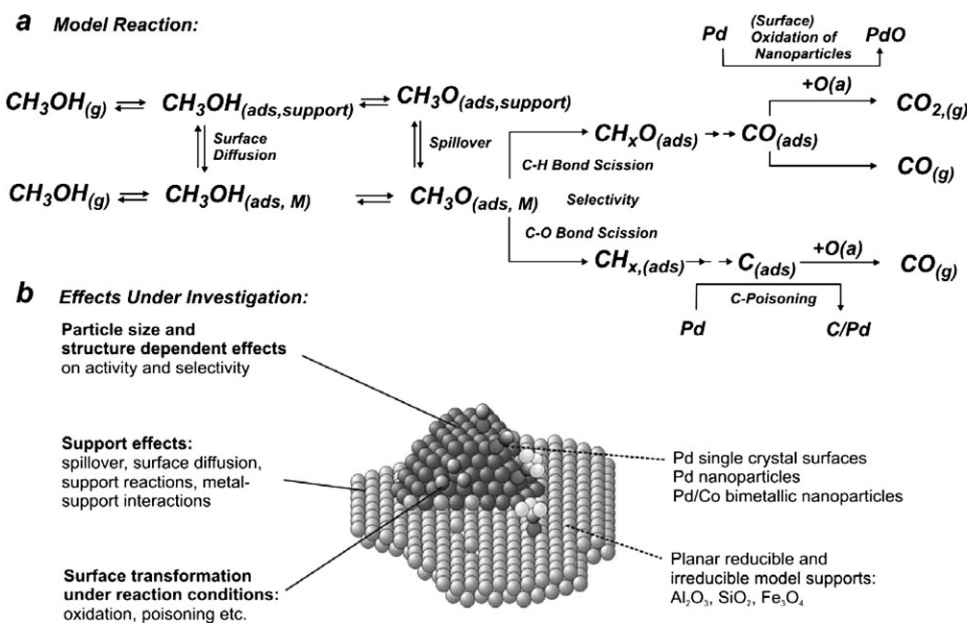

Fig. 1 (a) Methanol decomposition and oxidation on Pd model catalysts as a complex model reaction system, showing pronounced particle size, support and pressure dependent effects; (b) specific effects on the catalytic properties discussed in this study.

obtain a complete picture of the reaction system in spite of its apparent complexity.

(ii) Particle size and support effects

Studies of methanol synthesis and oxidation on real Pd based catalysts reveal pronounced particle size and support dependent effects.[30] These findings make model studies on related systems particularly promising, with the aim to identify the microscopic origins of such effects and, eventually, control the catalytic performance by structural and chemical modification. The corresponding experimental strategies will be discussed in section 5 (particle size and structure), section 7 (bimetallic particles) and section 9 (support effects).

(iii) Poisoning and oxidation under reaction conditions

Under reaction conditions, metal nanoparticles are rarely present in their clean and ideal state. Typical poisons, such as carbon, may accumulate on the surface, leading to deactivation, but also to characteristic changes in selectivity. In the presence of oxygen, there may be formation of oxides. In the special case of Pd particles, formation of surface and interface oxides phases may also occur (see, *e.g.*, ref. 37 and 38 and the references in section 8). Recently, the reactivity of these oxide phases has been controversially discussed (see, *e.g.*, ref. 39–42 and the references in section 8). We have investigated the formation of oxide phases under reaction condition as well as their reactivity in great detail. The corresponding results are reviewed in section 6 (carbon and oxygen at ambient pressure), section 8 (Pd oxide formation and activity) and section 9 (support effects and oxide formation).

3. The pressure gap: experimental approaches

Recently, large efforts have been made in order to develop experimental methods which allow structural and spectroscopic investigations over the full pressure range from UHV up to ambient conditions. This involves, for example, photon-based spectroscopic methods such as sum-frequency generation (SFG)[13–15,43,44] or polarization-modulation IR reflection absorption spectroscopy (PM-IRAS),[15–17,45] "high pressure photoelectron spectroscopy" (HP-PES) up to the mbar region,[21–23] the "environmental TEM" (E-TEM) which allows structural investigation in reactive atmosphere,[19,46] or scanning tunneling microscopy at high pressure (HP-STM) in reactor cells.[20,24]

In the collaborative project, which we are reviewing here, a broad range of experimental methods has been applied covering pressure regimes from UHV to ambient conditions. Under UHV conditions, we applied photoelectron spectroscopy (PES) also using synchrotron light sources (BESSY II, Berlin), temperature programmed desorption (TPD), IR reflection absorption spectroscopy (IRAS), scanning tunneling microscopy (STM), low-energy electron diffraction (LEED), and others. In the ambient pressure regime, kinetic studies were performed using reaction cells as batch reactors, which were compatible with *in situ* vibrational spectroscopy.[15,43] For model catalysts SFG and PM-IRAS were applied whereas for powder samples DRIFTS (diffuse reflectance infrared Fourier transform spectroscopy) was utilized. Gas phase analysis was performed by gas chromatography (GC) and/or mass spectrometry, as well as by photometric detection. Great efforts were made to link the UHV conditions and ambient world with a special focus on obtaining kinetic and spectroscopic information. For several experimental methods, we schematically illustrate in Fig. 2 the pressure range in which they were applied. To obtain detailed kinetic data, we performed multi-molecular beam (MB) experiments in combination with time-resolved IRAS.[47] The MB approach has been successfully applied to various reaction systems and is capable of providing detailed data on the microkinetics and dynamics of surface reactions under well-controlled conditions.[48–51] The application of MB methods to model catalysts was recently reviewed.[11] Pulse sequence MB experiments (PSMB) involving multiple beam sources as new experimental approach to complex reaction systems were recently discussed and applied to the oxidation and reduction kinetics of supported Pd nanoparticles.[52–54] For complex model catalyst surfaces, the combination of MB methods with surface spectroscopy (TR-IRAS in the present case) is of special importance, as it allows identification and monitoring of specific sites on the nanoparticle surface.[55]

Two spectroscopic methods were employed which specifically aim at bridging the pressure gap: SFG and PM-IRAS. Both methods can be applied from UHV to ambient pressure and are thus able to interconnect classical surface science studies with applied heterogeneous catalysis (for an overview see ref. 15). In particular, the overlap between MB methods and SFG/PM-IRAS for pressures around 10^{-6} mbar enables good correlations between these two approaches. The basics of SFG and PM-IRAS have been described in a number of previous articles (ref. 13, 15, 16 and 44 and references therein). Whereas nonlinear optical SFG spectroscopy is inherently interface specific, PM-IRAS allows for an accurate subtraction of gas phase contributions to yield surface vibrational spectra. Within the framework of this project the application of SFG to supported nanoparticles was established as a valuable tool to examine adsorbate phases at elevated pressure. The effect of particle size and gas pressure[14,44,56] on the site population and (co-)adsorbate phases,[57,58] as well as support effects[59] and fundamentals of SFG intensity and lineshape[60] was examined in detail. PM-IRAS allowed extending the frequency range and reducing acquisition times.[16,45]

Moreover, DRIFTS experiments were performed in a special, temperature-controlled reaction cell which was equipped with a controlled gas supply system and detection units for gas phase analysis at the exit side of the cell. This technique allows one to study powder samples *in situ* at ambient pressure by IR spectroscopy, provides a "pressure overlap" with the model studies, and allows a comparison with technically more relevant samples.

Combining the insight from kinetic studies, spectroscopy and theoretical results, microkinetic models were developed, which explicitly take into account various kinetic effects on nanostructured surfaces including the presence of different types of reactive sites, coupling of diffusion and reaction processes of formation and decomposition of oxide phases.[34,42,54,57,61–65]

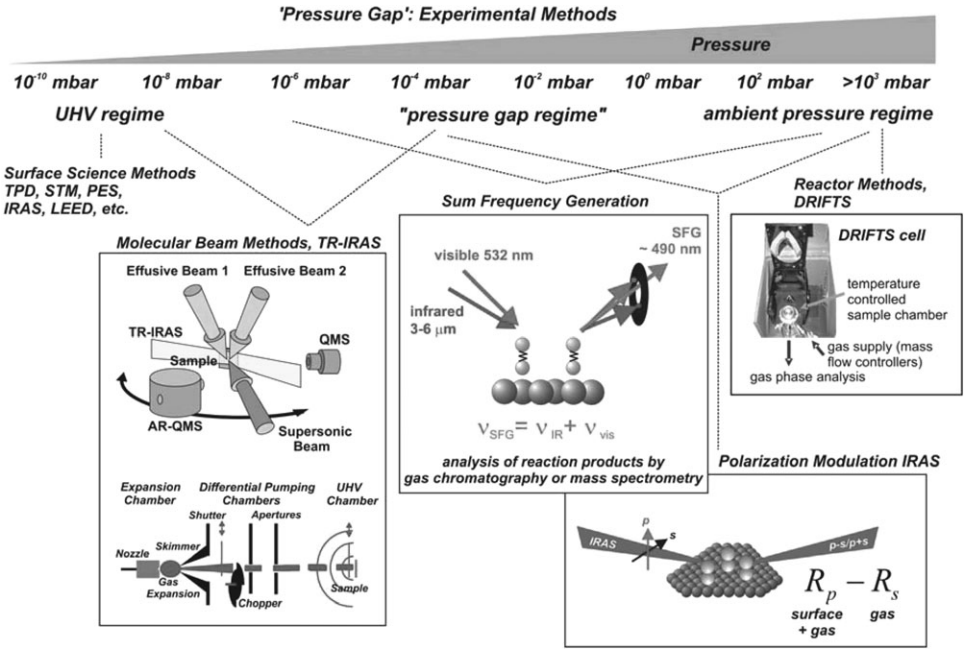

Fig. 2 Overview over experimental methods employed in this study: methods from surface science and heterogeneous catalysis are combined with experimental techniques bridging the ''pressure gap'' between them.

4. The materials gap: development of model catalysts

Real heterogeneous catalysts are highly complex materials, the chemical and structural surface properties of which are as difficult to control as to characterize. In contrast, surface science studies are best performed on single crystal surfaces, which are easily accessible to the full spectrum of experimental methods in surface physics and chemistry. In order to bridge this ''materials gap'', model catalysts were developed, which allowed us to introduce certain complex features of real catalysts in a well-controlled fashion, but—at the same time—to avoid the full complexity of the real system.[8,9,11,12,66] The development of these model systems is schematically illustrated in Fig. 3. In a first step, a well-defined oxide model support has to be prepared. Here, oxide single crystal surfaces and ordered oxide thin films can be employed. The latter provide the advantage that the full spectrum of surface science experimental methods including STM, PES and optical methods can easily be applied. In the present study, we used both reducible and non-reducible supports. As a non-reducible support we chose Al_2O_3 in the form of a thin ordered film on NiAl(110), which was characterized in detail both experimentally and theoretically.[67,68] As a reducible support, which is expected to interact more strongly with the active nanoparticles, we used Fe_3O_4 epitaxially grown on Pt(111).[69] Structure and adsorption properties of the Fe_3O_4 film were characterized as well.[69–71]

In the next step the active phase, *i.e.* the metal nanoparticles, is introduced, mainly by physical vapor deposition (PVD) of Pd under UHV conditions. By carefully controlling the deposition parameters, the particle size and density can be varied over a large range of values.[52,72–75]

Typically, average particle sizes between few atoms (<1 nm) up to several thousands of atoms (>10 nm) are available. Both on Al_2O_3/NiAl(110) and Fe_3O_4/Pt(111), the Pd particles grow in the form of ordered crystallites in (111) orientation, exposing preferentially (111) facets as well as a minor fraction of (100) facets (10–20%). For detailed structural parameters we refer to the literature.[52,73–75] Several types of reference and calibration experiments were performed on Pd(111) single crystal surfaces[16,45,76–78] and large Pd particles supported on SiO_2/Si(100) prepared by means of electron beam lithography (in cooperation with A. Grant and B. Kasemo, Göteborg, Sweden).[63–65,79]

In the final step, the complexity of the model catalyst is further increased, *e.g.* by surface modification or by introduction of additional active components, poisons or promoters. Here, we pursued three directions: first, we investigated the modification of the adsorption and reaction behavior by alloying, focusing primarily on bimetallic PdCo particles (see section 7). Secondly, we considered the poisoning of the particles by carbon under UHV and ambient conditions (sections 5 and 6). Finally, we investigated the influence of oxidation or partial oxidation of the particles (sections 8 and 9).

On the first route towards more complexity, bimetallic PdCo model catalysts were generated by subsequent PVD of Co and Pd on Al_2O_3/NiAl(110) in UHV. Taking advantage of the different surface mobility of Pd and Co, a homogeneous distribution of hemispherical Co core-Pd shell particles with diameters in the range 2–3 nm can be obtained when Co is deposited first and Pd second.[80,81] Depending on the relative amount of Pd and Co, the particle composition can be tuned from Co decorated by surface Pd atoms to a Co core with a complete Pd shell, while the particle density and overall shape

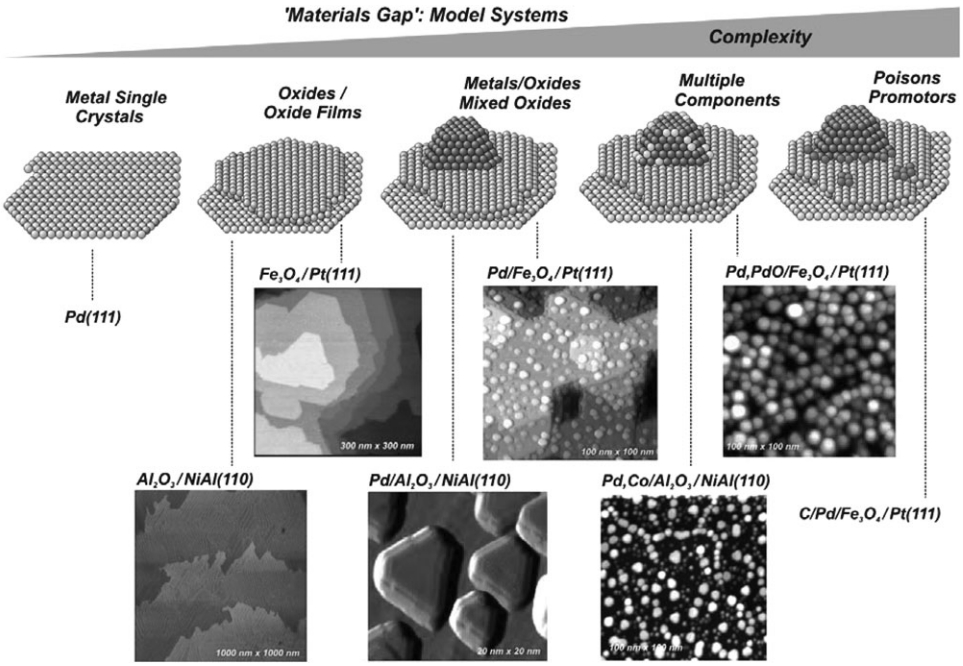

Fig. 3 Model catalysts of increasing complexity are developed in order to bridge the "materials gap" between surface science and heterogeneous catalysis. The figure shows STM images of model systems used in this study (see text), from ref. 53, 140–142.

remain unaltered. With deposition at 300 K, one typically obtains particle densities in the range of 9×10^{12} cm^{-2}. Moreover, efforts to overcome the materials gap were also undertaken coming from the side of real catalysts. Therefore, MgO supported, mono- and bimetallic Pd and Co–Pd model catalysts were prepared by controlled decomposition of metal acetylacetonate precursors on MgO. Fig. 4 shows HRTEM images of monometallic Pd/MgO and bimetallic Co–Pd/MgO catalysts.[82,83] The average particle size is $\sim$6 nm for Pd and $\sim$4 nm for Co–Pd. The nanoparticles grow in defined epitaxial relations on the support: the (001) face of the particles is parallel to the (001) face of the MgO support, with the [100] axes of the nanoparticles being parallel to the [100] axes of the MgO lattice. Furthermore, the nanoparticles possess well-defined facets. The shape can be described by an octahedron with (111) facets where the corners are truncated by (100) facets.[82] Thus, these systems exhibit a number of well-defined structural features which makes them suitable for model catalytic studies under ambient conditions.

For understanding of the experimental results at a microscopic level, a close interaction with theory is essential. Nevertheless, even the model catalysts are too complex for a first-principles theoretical treatment. Therefore, a modelling strategy was proposed and developed[84] to represent at a sufficiently realistic level oxide-supported nanoparticles with $\sim 10^3$ metal atoms, which are experimentally explored as model catalysts.[11,15,85] This novel approach employs ordered 3-D nanoparticles with structures cut from bulk metal and terminated by low-index surfaces. Any direct influence of the oxide support on the adsorption properties and the reactivity of the metal nanoparticles is neglected; this latter approximation is easily justified in many experimental situations. Cases where chemical reactions directly involve the metal–oxide interfaces were not dealt with in this project; they would require special tailor-made models.[86,87] Most of our theoretical studies were performed at the all-electron scalar-relativistic level, using the linear combination of Gaussian-type orbitals fitting-functions density functional (LCGTO-FF-DF) method[88] as implemented in the parallel code *ParaGauss*.[89,90] The present work aimed at modelling the reactivity of metal particles in a size range where cluster properties are scalable to the bulk.[91,92]

A series of (cub-)octahedral clusters Pd_{55} to Pd_{146}, with the geometry fixed as in Pd bulk, was calculated focusing on the interaction of CO with threefold hollow sites on Pd(111) facets.[84] That study examined how different adsorption parameters vary with cluster size and how these values of cluster models relate to the adsorption properties of the corresponding site at the Pd(111) surface. Starting from the model Pd_{79}, the calculations yielded CO adsorption energy varying in a range spanning 5 kJ mol^{-1} only.[84] Thus, nanoscale models

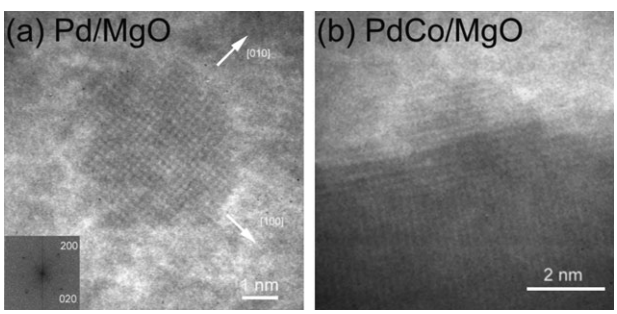

Fig. 4 HRTEM images (taken by S. Giorgio and C. Henry, Marseille) of (a) monometallic Pd and (b) bimetallic CoPd nanoparticles on MgO. In (a) the particle is seen in a top view along the [001] axis; in (b) a profile view along the [100] axis is shown.[83]

consisting of ~80 Pd atoms basically no longer exhibit size effects in regard to adsorption properties. This very important finding indicates that reasonable convergence of adsorption energies on a single-crystal metal surface can be reached with moderately large compact cluster models, which avoid the drawbacks of conventional cluster models where a significant fraction of metal atoms at the boundaries is insufficiently coordinated. The adsorption energy from the "converged" cluster models is essentially in *quantitative* agreement with energies calculated from periodic slab models, provided the same exchange–correlation functional is used in both calculations. Moreover, these cluster models enable a realistic description of adsorption properties and reactivity of metal particles in supported model catalysts. "Nanocrystal" models comprising up to a hundred atoms (or even more) can be chosen to exhibit computationally advantageous (but not mandatory) high point group symmetry.[93]

5. Microscopic origins of particle structure and particle size effects

As a first step, we investigated the relationship between particle structure and selectivity, scrutinizing the decomposition of methanol on Pd/Al_2O_3 model catalysts. Our experimental and theoretical strategy may be summarized as follows.[35,55,94–100] First, a spectroscopic identification of the different adsorption and reaction sites on the Pd nanoparticles is established. Secondly, the rates of the two competing reaction channels, C–H and C–O bond breaking of methoxide, CH_3O, are determined in dependence of the occupation and availability of the different sites. Finally, the results are interpreted on the basis of theoretical calculations.

The spectroscopic identification of different types of adsorption sites on supported particles is not straightforward because even well-shaped nanoparticles expose several different sites, the spectroscopic properties of which are often similar. Here the intrinsically high "chemical resolution" of IRAS turned out to be very helpful, allowing us to use CO as a sensitive probe molecule. As shown for both the planar model catalysts and powder samples, the absorption spectra in the CO stretching frequency region provide detailed information on the particle morphology and size.[14,44,58,73,95,96,98,101–103] The situation is complicated by the fact that the spectra are strongly modified by dipole coupling phenomena and the nanoparticles often expose sites for which there is no single-crystal reference data. On the basis of DFT cluster calculations, however, it was possible to assign specific bands in CO stretching frequency region to specific nanoparticle sites.[95]

Among the CO adsorption sites studied on Pd cluster models of about 140 atoms, were threefold hollow, bridge, and on-top positions at (111) facets, fourfold hollow and on-top sites at (001) facets, bridge positions at cluster edges as well as on-top positions at cluster corners and on single Pd atoms deposited at regular (111) facets.[95] The strongest CO bonding was determined for bridge sites at cluster edges. The adsorption energy atop low-coordinated Pd centers (kinks) was also calculated larger than that for sites atop the (111) and (001) facets. Characteristic absorption accompanying CO adsorption was also calculated for vibrations of bridge-bonded CO at edges and defects of particles.

Experimentally, we observed a dominating band for $CO/Pd/Al_2O_3$ between 1950 and 1970 cm^{-1},[14,44,55,95,101] which, on the basis of the above calculations,[95] we primarily assigned to bridge bonded CO at particles edges, together with minor contributions from bridge bonded CO at steps and on (100) facets. It was found that upon carbon accumulation on the Pd particles as a result of C–O bond scission of methanol, these edge sites (in addition to the step and (100) sites) are preferentially blocked.[55,94]

This finding allowed us to compare reaction rates for C–H bond scission and C–O bond scission on clean and on carbon modified Pd particles, in order to obtain information on the site dependent reaction rates. The corresponding MB experiments are summarized in Fig. 5. First, we measured the rate of C–H bond scission by monitoring the formation rate of CO as a dehydrogenation product. This can be performed by means of an isotope exchange experiment, switching between $^{12}CH_3OH$ and $^{13}CH_3OH$ beams of equal intensity and simultaneously monitoring the CO absorption signal by TR-IRAS. In Fig. 5a the corresponding average CO stretching frequencies are displayed as a function of time, for both the clean and the partially carbon covered sample. Apparently, the kinetics of CH_3OH dehydrogenation to CO is similar on both samples, indicating that the rate of C–H bond scission shows only a weak dependence of the reaction site.

Next we focused on the rate of C–O bond scission, which is an intrinsically slower reaction under UHV conditions. The rate can be easily measured by means of a TR-IRAS experiment, exposing the sample to a continuous CH_3OH beam. C–O bond scission leads to slow accumulation of C species on the particle surface, blocking the corresponding sites for CO adsorption. As a result, the CO absorption signal decreases as a function of exposure time. As the CO IRAS bands nonlinearly depend on the coverage (mainly due to dipole coupling effects),[104,105] coverage calibrations of the signal were performed, combining TR-IRAS with sticking coefficient measurements. The experimental result is displayed in Fig. 5b. In contrast to the behavior observed for C–H bond scission, it was found that on the clean particles C–O bond scission is significantly faster than on the partially C-poisoned particles.

In summary, we may conclude that—independently of the reactive site—C–H bond scission (*i.e.* dehydrogenation leading to CO) represents the dominating reaction channel. The rate of C–O bond scission (leading to formation of carbonaceous species) is slow but strongly depends on the type of active site. The reaction was found to be significantly enhanced at edge, (100) and defect sites. As a result, the selectivity strongly differs for the different active sites and, therefore, is expected to depend on particle shape.

To corroborate these experimental findings and to identify the reaction pathways, density functional (DF) calculations were carried out. We theoretically investigated C–O bond cleavage of the key intermediate methoxide, in comparison with the corresponding first dehydrogenation step. On a regular Pd(111) surface, we found dehydrogenation of CH_3O to CH_2O to be clearly preferred to C–O bond breaking, for both thermodynamic and kinetic reasons,[106] in line with

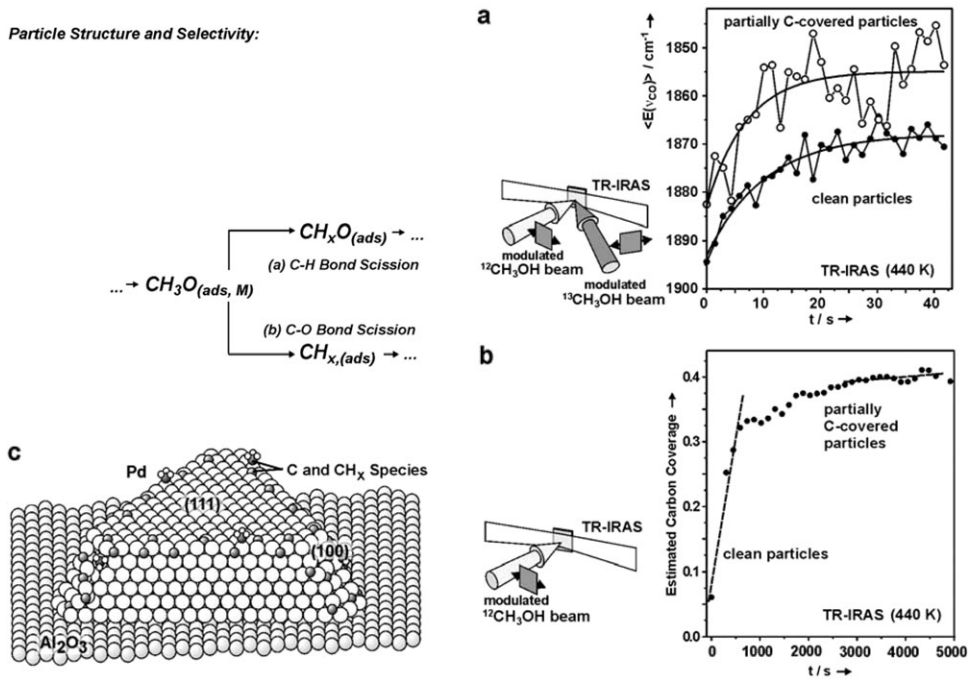

Fig. 5 Molecular beam experiment showing the relationship between particle structure and selectivity during methanol decomposition on Pd nanoparticles on Al_2O_3/NiAl(110). Methanol decomposition proceeds *via* two competing reaction channels, C–O bond scission and C–H bond scission (see text). (a) An isotope exchange TR-IRAS experiment provides information on the kinetics of C–H bond scission as a function of carbon poisoning of the surface. (b) A MB/TR-IRAS experiment provides information on the rate of C–O bond scission (see text for detailed discussion), from ref. 55.

observations in the present experimental studies. We calculated dehydrogenation to be exothermic by 45 kJ mol^{-1} in contrast to the slightly endothermic C–O bond scission (by 5 kJ mol^{-1}). The corresponding calculated activation barriers, 33 and 146 kJ mol^{-1}, respectively, indicate that C–O bond scission of CH_3O on Pd(111) surface is very slow compared to C–H activation.[106] To explore whether the reactivity of model catalysts can be different because these nanoparticles exhibit defects (*e.g.* edge sites), we theoretically studied C–O bond scission of methoxide intermediates adsorbed on Pd nanoparticles.[93] A ''round'' Pd_{79} nanocrystallite (O_h symmetry without adsorbate) was chosen to represent model catalysts built of well-ordered supported Pd particles. The overall symmetry of the models was reduced to D_4, to allow modelling of different location modes of adsorbed intermediates as well as of the transition state for C–O bond scission of CH_3O. That study employed for the first time a strategy based on models without any *local* geometry restriction; still, adsorbed species were symmetrically deposited at all eight (111) facets of cuboctahedral clusters.

The calculated structures involved in the process under scrutiny are displayed in Fig. 6, together with pertinent calculated energy values.[93] Residual CH_3, which arises from C–O bond breaking of CH_3O, was determined to be most favorably adsorbed in the on-top position at a cluster edge between two (111) facets, ~20 kJ mol^{-1} more stable than on the (111) facets. The other reaction product, oxygen atoms, remained strongly bound at (111) facets of the Pd cluster. Because CH_3 species are stabilized at cluster edges, the scission of C–O bond was calculated to be exothermic on nanoclusters, by ~40 kJ mol^{-1}. However, the rather high calculated activation barrier, 138 kJ mol^{-1}, implies that methoxide decomposition on Pd *via* the C–O bond breaking route proceeds very slowly, even on edge sites.

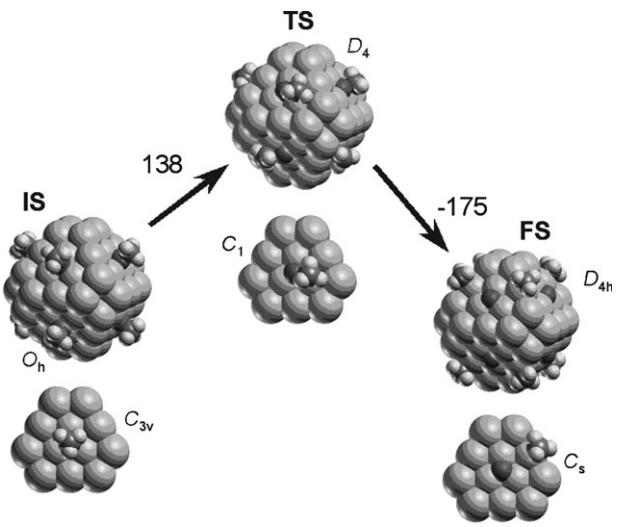

Fig. 6 Methoxide decomposition on the cluster model Pd_{79}. General view of the cluster with adsorbate (upper panels) and top view of a single (111) facet (lower panels): initial state (IS) with CH_3O adsorbed at the central fcc site of a (111) facet (O_h total symmetry), transition state (TS) for C–O bond scission (D_4), final state (FS) with oxygen at central fcc site and methyl at the edge of the cluster (D_{4h}). The energy differences are in kJ mol^{-1}.

6. Influence of poisons from UHV to ambient conditions

Thus, under typical UHV conditions and low pressures (MB conditions), C–O bond scission is only a minor pathway (see also ref. 45 and 107 and references therein), preferentially occurring on specific sites (as discussed above) and not on (111) terraces. This may change when pressures of $\sim 10^{-6}$ mbar or higher are applied and when exposure times are longer. Under such conditions the contribution of C–O bond scission becomes stronger, leading to the formation of carbonaceous overlayers and to catalyst deactivation.[16,99,107] Fig. 7 summarizes results on CH_3OH decomposition on Pd(111) and Pd nanoparticles supported by Al_2O_3, acquired by XPS and SFG (at 300–400 K). Fig. 7a shows the kinetics of CH_x formation on Pd(111) as obtained from XPS (for the spectra see ref. 107). At 400 K and 5×10^{-7} mbar a CO coverage of ~ 0.2 ML is instantly established but even on smooth Pd(111) ~ 0.7 ML CH_x were produced within about 4 h. Using CO as probe molecule to examine the surface before and after methanol exposure (lower and upper trace in Fig. 7b, respectively) indicated that preferentially hollow sites were poisoned by CH_x. Whereas before the reaction the typical (2×2)-3CO structure was observed (with hollow and on-top bonded CO at 1898 and 2109 cm^{-1}, respectively[56]), after methanol exposure the intensity of hollow and on-top CO decreased and CO adsorption at bridge sites was observed (for a detailed discussion see ref. 107). At higher CH_3OH pressure (up to 0.1 mbar) the CH_x amount increased leading to successively stronger poisoning of hollow (and on-top) CO adsorption (immediate poisoning of any CO adsorption after exposure to 0.1 mbar at 400 K).[107]

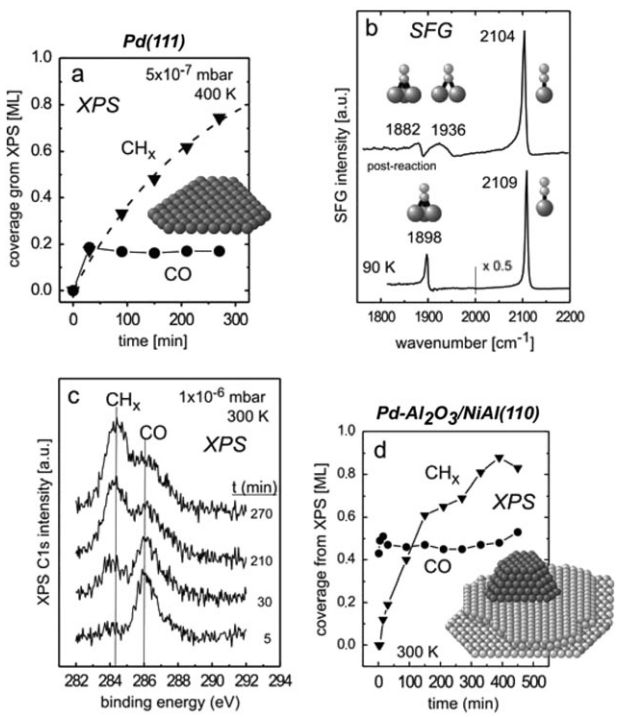

Fig. 7 SFG and XPS measurements during CH_3OH decomposition on (a), (b) Pd(111) and on (c), (d) Pd particles supported on Al_2O_3. SFG spectra of a CO saturation coverage on Pd(111) before (lower trace) and after (upper trace) methanol exposure are compared in (b), from ref. 99 and 107.

Under similar pressure conditions, CH_3OH exposure to Pd nanoparticles also led to a strong poisoning due to CH_x formation (Fig. 7c, d). Compared to Pd(111) the poisoning effect is probably even stronger and exposure to 1×10^{-6} mbar CH_3OH at 300 K produced ~ 0.7 ML CH_x within 4 h. Thus, the Pd particles rapidly deactivated and CH_3OH decomposition at pressures up to 50 mbar and temperatures up to 450 K did not yield any decomposition products, as indicated by GC. Apparently, a reaction route that is only a minor pathway under UHV conditions (or when the very initial states of a reaction are considered) may become dominant under elevated pressure conditions.

To understand the reactivity effect of the deposited carbon species on Pd nanoparticles, data on the relative energies of various surface positions of these species are very helpful. For a series of conceivable adsorption sites on the nanoparticle model Pd_{140} of cuboctahedral shape, we theoretically characterized C–Pd_n interactions structurally, energetically, and from the viewpoint of adsorbate–substrate charge rearrangement.[108] The C atoms were calculated to be strongly adsorbed in the form of carbidic species that bear a significant negative charge and thus experience notable mutual electrostatic repulsion at short distances. Surface sites with fourfold coordination (the highest possible) of C appear to be overall favored; on the (111) facets, threefold hollow sites in the center are energetically preferred. Reducing the global symmetry of the nanoclusters from O_h to D_{4h} point group allowed us to study selected locally less-symmetric adsorption complexes, which feature notably diminished intra-adsorbate electrostatic repulsion. In such D_{4h} models, displacement of adsorbed C toward the borders of a facet was accompanied by a slight destabilization. We did not find any energy gain due to enhanced C-substrate interactions at regular sites near the boundaries (edges) of (111) facets. In light of our theoretical work,[93] one may propose the following scenario of accumulation of C deposits near the edges of Pd particles, which is in agreement with the experimental findings.[55] At regular sites and, somewhat faster, near the edges of Pd clusters, adsorbed CH_3O species decompose very slowly to adsorbed CH_3 and O species. CH_3 moieties at edges are ≥ 20 kJ mol^{-1} more stable than congeners adsorbed at other sites, which drives the migration of CH_3 to cluster edges. There, methyl adsorbates are dehydrogenated to C species, which are rather immobile[108] and, thus, preferably stay at the edges where they were formed.

Carbon species appear to be small enough to probe subsurface interstitial positions as an alternative to surface deposition; the local structure of such impurities is reminiscent of carbon-centered organometallic cluster compounds[109] and products of their partial decomposition on oxide supports.[110] To model such (and related) species, we performed DF calculations on nanosize cluster models of Pd catalysts with surface and subsurface impurities of light atoms H, C, N and O.[111] Single atoms adsorbed at threefold hollow sites in the center of each of the eight hexagonal (111) facets of the cuboctahedral clusters Pd_{79} or Pd_{116} were allowed to "migrate" to octahedral or tetrahedral subsurface sites from

the fcc or hcp surface hollow sites, respectively. These models provided insight into the relative stability of surface and subsurface atomic species as well as the corresponding activation barriers for migration to subsurface positions. Among the atoms considered, only carbon in the subsurface octahedral interstitial position beneath the Pd(111) facets was found to be stabilized with respect to the corresponding surface position. A moderate activation barrier of $\sim$60 kJ mol^{-1} for the diffusion of atomic C from surface fcc sites to octahedral subsurface sites indicated noticeable propensity of carbon to occupy a subsurface position on Pd(111).[111] Interestingly, subsurface carbon underneath (111) facets of the cluster Pd_{79} is stabilized by only 14 kJ mol^{-1} compared to its surface position,[111] whereas the corresponding calculated stabilization on the Pd(111) surface of extended samples is noticeably larger.[112] This very important finding illustrates that metal nanoparticles, even large enough to feature adsorption parameters very close to those of surfaces of bulk metal,[84] can exhibit a reactivity different from that of the latter systems because the propensity for surface-to-subsurface diffusion is noticeably different.

Effects of subsurface carbon impurities on the reactivity of Pd catalysts can be monitored using adsorbed CO molecules as probes in the vicinity of the impurities. A key for rationalizing the influence of such subsurface atoms on Pd is the carbidic nature of subsurface C,[111,112] with a large negative charge of $\sim$1 *e*, similarly to that of the surface C deposits.[108] This accumulation of electron density at C impurities should notably limit electron back donation from the metal to the antibonding $2\pi^*$ orbital of a nearby CO adsorbate, hence destabilize such adsorption complexes. Results of DF calculations confirmed this expectation: CO adsorption is destabilized by $\sim$50% at fcc sites directly above the subsurface interstitial C moiety.[108] This destabilization slowly decreases at more distant hollow sites, but still remains substantial for adsorbates at distances of 0.4 nm and beyond from the impurity.[112] This computational result is at variance with the conclusion derived from STM experiments, that subsurface impurities on Pd(111), tentatively assigned as interstitial atomic carbon species, are able to *stabilize* nearby CO adsorption.[113] Apparently, further experimental work in combination with accurate calculations is required to characterize unequivocally the nature of such impurity species at Pd(111). Such a joint effort is expected to contribute to a more detailed understanding of metal systems with subsurface impurities in general.

7. Controlled modification of adsorption and activity on bimetallic nanoparticles

In general, the preparation of *bimetallic* catalysts offers additional possibilities to influence important characteristics like the activity and selectivity.[80,81,114,115] In the context of Pd catalysts for methanol decomposition, we examined the influence of Co as a second metal. Experiments were performed on two types of model catalysts. On the one hand, wet-chemically prepared, but nevertheless well-defined metal nanoparticles on MgO supports were studied under ambient conditions, as a model system close to real catalysts (see also section 4). On the other hand, experiments under UHV conditions were performed on well-defined, bimetallic Co–Pd nanoparticles prepared on Al_2O_3/NiAl(110) by PVD. This approach addressed both the pressure and the materials gap.

On both types of model catalysts, *i.e.*, in UHV and at ambient conditions, CO adsorption as a probe for available surface sites revealed significant differences between mono- and bimetallic particles. The results of CO-TPD and FTIR studies at the model catalysts in UHV are shown in Fig. 8 for various PdCo particle compositions, including pure Co and Pd particles. Please note that the amount of deposited Co and Pd is given as average thickness (in Å) of a reference layer of the respective metal. For the formation of a complete Pd shell on an ensemble of Co particles, the deposition of about 2 Å Pd on

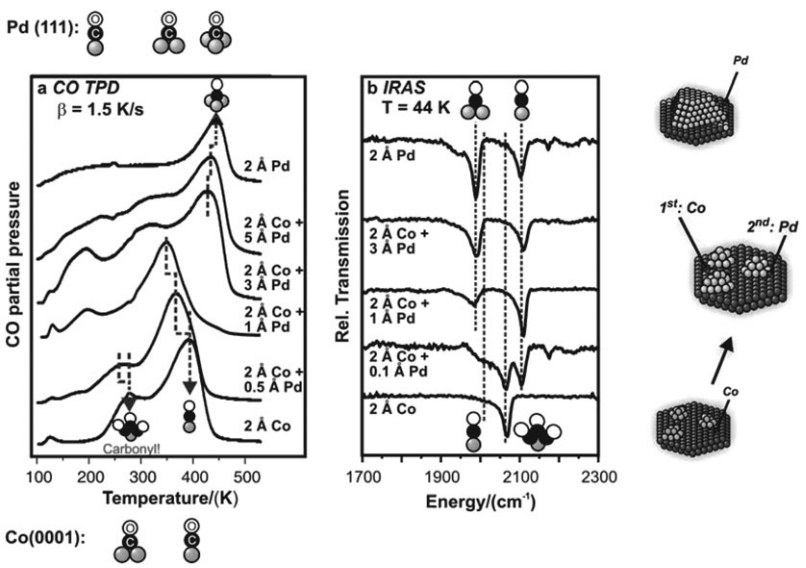

Fig. 8 (a) CO-TPD spectra for various bimetallic particle compositions. The notation 2 Å Co (Pd) denotes the amount of deposited material as average thickness of a reference metal layer. (b) Collection of IR absorption spectra for CO saturation coverage on various bimetallic PdCo particle compositions.

top of 2 Å Co is required. At lower Pd coverage the shell remains incomplete.

For pure Pd, CO is bound preferentially at threefold hollow sites, identified by the TPD peak at 450 K. In contrast, CO prefers on-top positions on Co, represented by the TPD signal at 390 K (Fig. 8). The binding energy on both Pd and Co is lowered as soon as the second metal is present, indicating significant ligand and ensemble effects.[80,116,117] Apart from the atop-bound CO, TPD revealed a second CO species on Co, with a desorption maximum at ~280 K and a clear fingerprint at 2068 cm^{-1} in FTIR spectra taken at 44 K. Based on a careful analysis involving isotope exchange experiments,[118] the band at 2068 cm^{-1} was attributed to a Co carbonyl species, probably forming at low-coordinated Co sites. It is noteworthy that, although CO in on-top positions is the predominant species (see TPD), it is hardly detected in the IR spectra because of an exceptionally strong dynamical dipole moment of the carbonyl species.[118] After adding Pd to the Co particles, the IR intensity of the carbonyl species strongly decreased indicating that Pd on the Co particle surfaces first decorates these Co-carbonyl sites. At Pd coverage well below 2 Å, the IR band of the carbonyl was finally completely quenched.

Comparing the UHV and the ambient condition systems, a number of similarities regarding the CO adsorption behavior can be noticed. In Fig. 9a, b, DRIFTS data are presented for monometallic Pd and bimetallic Co–Pd nanoparticles on MgO, respectively, which were exposed to a continuous flow of 0.1 vol% CO in Ar at ambient pressure. Here, in the case of pure Pd nanoparticles with an average size of ~6 nm, CO adsorption at room temperature resulted in the appearance of three IR bands in the carbonyl stretching region at ~1904, ~1983 and ~2063 cm^{-1} which correspond to CO on threefold hollow sites, bridge-bonded CO and linearly bonded CO, respectively.[82] In comparison, the FTIR data for Pd particles in UHV showed bridge-bonded CO in nearly perfect agreement at ~1986 cm^{-1} but linearly bonded CO at 2104 cm^{-1}. While the latter species is located on Pd(111) terrace sites in the UHV experiments, it was found that the band at ~2063 cm^{-1} observed at ambient pressure corresponds to linear adsorption of CO on edges of the well-shaped Pd crystallites.[82] In contrast to the UHV experiments at low temperature, CO adsorption in linear configuration was not saturated in the continuous-flow experiments at room temperature leading to a situation that resembles spectra below saturation coverage in CO dosage experiments on Pd particles in UHV (*cf.* ref. 44 and 119). Note, however, the weak shoulder around ~2100 cm^{-1} (see Fig. 9a) indicating at least a small contribution of CO on (111) facets in the considered ambient temperature and pressure regime.

It should be noted here that the FTIR bands observed at 1983 and 1986 cm^{-1}, respectively, are ascribed to bridge-bonded CO at *particle edges and steps*.[118,119] In the UHV

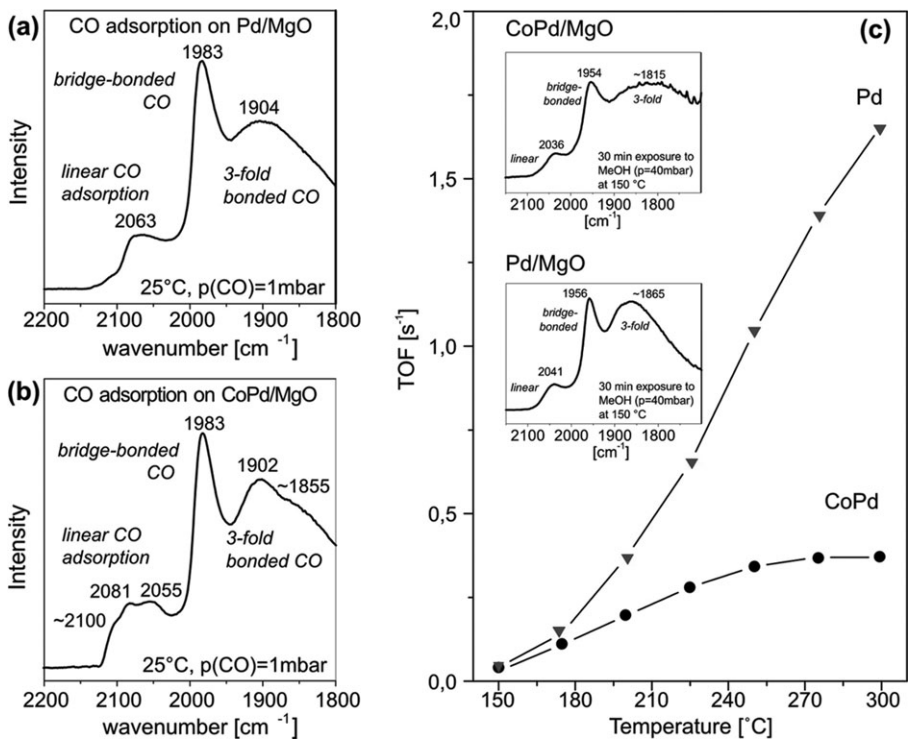

Fig. 9 (a), (b) IR spectra of monometallic Pd (a) and bimetallic Co–Pd nanoparticles (b) on MgO after exposure to a continuous gas flow of $0.1\%_{vol}$ CO in Ar at room temperature. The spectra are referenced to background spectra recorded before exposure to CO. (c) Study of methanol decomposition on well-defined Pd and CoPd particles supported on MgO under continuous flow conditions in a lab reactor (40 mbar methanol in Ar). The traces show the turn over frequencies of CO formation (calculated on the basis if the steady state yield and the particle size) as a function of temperature. The insets contain IR spectra of the catalysts under reaction conditions recorded by DRIFTS (note that for both the Pd and PdCo particles, small amounts of CO_2 were detected as a by-product in analogy to other studies of methanol decomposition on supported Pt and Pd catalysts.[143,144])

experiments, there is also a shoulder visible in the frequency range at around 1950 cm^{-1} (see Fig. 8b) which is typical of bridge-bonded CO on *terrace sites* of the (111) facets. Since IR intensities must not be taken as an absolute measure of coverage, the relative abundance of the different bridge-bonded species on the Pd particles can not be estimated from the IR spectra.

In the case of the bimetallic Co–Pd model catalysts, DRIFTS showed three bands in the region corresponding to linearly bonded CO with stretching frequencies of $\sim$2055, 2081 and $\sim$2100 cm^{-1}, respectively (Fig. 9b). Whereas the bands at $\sim$2055 and $\sim$2100 cm^{-1} can again be assigned to linear adsorption of CO on Pd edge and facet sites, the band at $\sim$2081 cm^{-1} which was easily removed by heating to only $\sim$100 °C, can be attributed to the Co carbonyl species, also detected in the UHV experiments. An additional band appeared in the region of threefold bonded CO at $\sim$1855 cm^{-1} which might be due to CO on hollow sites with bonds to Pd *and* Co atoms.[83]

In comparison, experiments in UHV and under ambient conditions showed similar results with respect to CO adsorbate species on the bimetallic model catalysts. It will be demonstrated in the following that they also exhibit similar trends for the decomposition of methanol.

FTIR studies of methanol adsorption on the Pd/MgO model catalyst revealed that methanol can be efficiently dehydrogenated to CO on the powder system in contrast to the particles on the alumina film at elevated pressures (section 6). Even at room temperature, IR bands corresponding to CO adsorbed on Pd were observed after exposure of the supported catalyst to methanol with a partial pressure of $\sim$40 mbar.[83] The inset in Fig. 9c shows an IR spectrum after exposure at 150 °C, where three bands corresponding to linearly, twofold and threefold bonded CO are clearly discernible. Analysis of the gas phase in catalytic test reactors revealed a strong temperature dependence of the CO formation. In Fig. 9c the turn over frequencies (TOF) calculated on the basis of the particle size and morphology are displayed as a function of temperature. Up to 150 °C, the TOF for CO formation was very low. At higher temperature, the activity increased continuously, reaching a value at 250 °C that is by a factor of $\sim$40 higher than at 150 °C. For all temperatures, higher CO yields were achieved if the methanol used was totally free of water.[83] This is expected since the reaction of methanol with water ($CH_3OH + H_2O \rightarrow CO_2 + 3H_2$) or subsequent water gas shift should diminish the CO yield. The activity of the powder system for methanol decomposition might be surprising in view of the carbon poisoning (deactivation) of the single crystal based model system discussed in section 6. This suggests that at higher reaction temperature (above 475 K) carbon poisoning has a smaller effect (the TOFs remained constant over 12 h), most likely due to a removal of CH_x during the reaction, *e.g. via* reaction to CH_4.

A similar overall behavior was observed for the bimetallic Co–Pd/MgO model catalyst. Also in this case, IR spectra of the carbonyl stretching range (inset in Fig. 9c) revealed adsorbed CO as a decomposition product of methanol adsorption. IR bands were weak at room temperature, but well pronounced at temperatures above 100 °C. For higher temperatures, the turn over frequencies (Fig. 9c) increased in a similar way as observed for the monometallic Pd particles.[83] The absolute values, however, were lower by a factor of $\sim$2–4.

To study the decomposition of methanol on the model catalysts in UHV, these were exposed to 15 L methanol at 115 K before TPD was performed up to 550 K. Desorption of methanol multi-layers detected at temperatures below 150 K was taken as evidence that the surface had been saturated with CH_3OH. In Fig. 10 CO-TPD spectra are presented for pure Co and Pd particles as well as for all bimetallic particle compositions studied. C–H scission is the major route for methanol decomposition irrespective of the particle composition, as indicated by a strong CO signal in all TPD spectra. In accordance, XPS revealed only minor carbon residues after a TPD run, as expected if a C–O-scission is less favored. CO desorption maxima were observed in the range from 380 to 450 K, in good agreement with the desorption temperatures

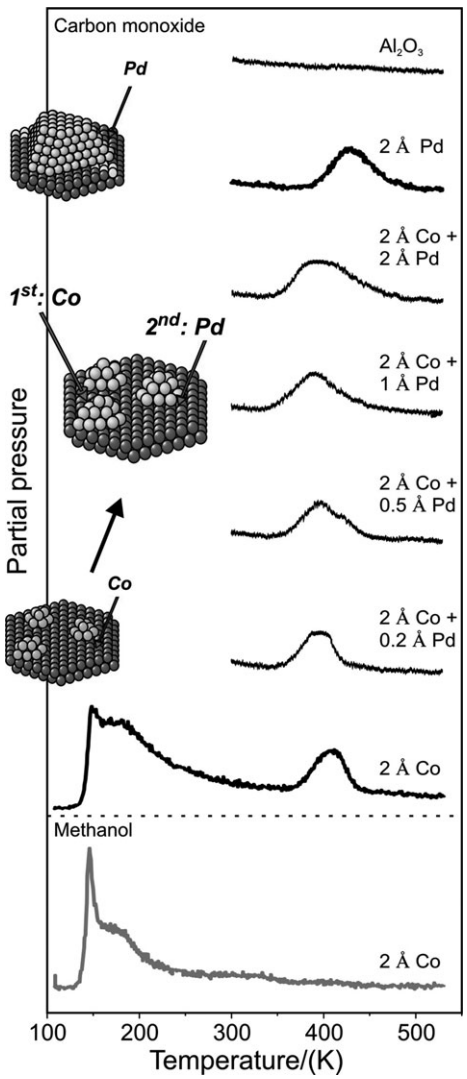

Fig. 10 TPD spectra recorded for Pd, Co and bimetallic PdCo particles of various compositions after saturation with methanol at 115 K. The upper spectra show mass 28 (CO), whereas the lowest spectrum shows mass 32 (methanol). The comparison for pure Co particles shows that features in the CO spectra below 300 K are due to the contribution of the cracking pattern of methanol to mass 28.

observed for the bimetallic particles in the CO adsorption experiments (compare Fig. 8). Consequently, at lower temperatures, methanol decomposition must be limited by CO desorption, which explains why the experiments at ambient conditions detected significant amounts of CO in the gas phase only at elevated temperatures although CO formation was observed on the surface by IR spectroscopy already at lower temperatures.

In order to obtain a measure for the activity of the UHV model catalysts of different particle compositions for methanol decomposition, the CO TPD signals were integrated and normalized to the metal particle surface area. A comparison revealed that the total CO yield per particle surface area is highest for the pure Pd particles and decreases for the bimetallic compositions. (Note that the TPD intensities for the Pd and bimetallic particles are comparable, but the number of surface atoms is significantly lower for the large Pd crystallites.) For pure Co particles the activity is at its lowest value. In accordance with the observations at ambient conditions in the reactor, bimetallic PdCo particle compositions thus lead to a reduction of methanol decomposition activity to CO, when compared to pure Pd particles. This is in contrast to studies on methanol decomposition at Co layers on Mo(110) where no bimetallic effects were detected.[120]

8. Oxidation and reduction of nanoparticles under reaction conditions

A special complication arises for reactions on Pd and other noble metal based catalysts in the presence of oxygen. The interaction of oxygen with the Pd surface turns out to be rather complex, involving the formation of various chemisorption structures, followed by the incorporation of subsurface oxygen into the first metal layer, the generation of surface oxides and finally the formation of bulk oxides. The structure and activity of the numerous oxide derived structures and phases has been the subject of intense experimental end theoretical work for several decades.[37,38,121–133] Recently, the structure of surface oxides on Pd(111) and Pd(100) could be solved by a combination of experiment and theory.[37,38] However, the activity of these and other oxide phases is controversially discussed.[39,40,42] On supported particles, the situation is further complicated due to the simultaneous presence of multiple sites (different crystallite facets, edges, corners, defects *etc*.), lattice distortions, modified electronic structures of small particles and due to possible interactions with the support.

In order to probe the effect of particle oxidation on the catalytic activity we have performed systematic MB studies on the kinetics of oxide formation, decomposition and on the mechanism of oxidation reactions on partially oxidized supported model catalysts.[41,52–54,74,134–136] The experimental setup and procedure are schematically shown in Fig. 11a: The Pd/Fe_3O_4 model catalyst is exposed to a programmed sequence of gas pulses (CO and $^{18}O_2$), simultaneously monitoring the CO_2 production rate and adsorbed CO *via* TR-IRAS. The results of a simple pulse sequence molecular beam (PSMB) experiment of this type are displayed in Fig. 11b. Initially, the fully reduced Pd/Fe_3O_4 sample was exposed to an extended O_2 pulse at different surface temperatures, followed

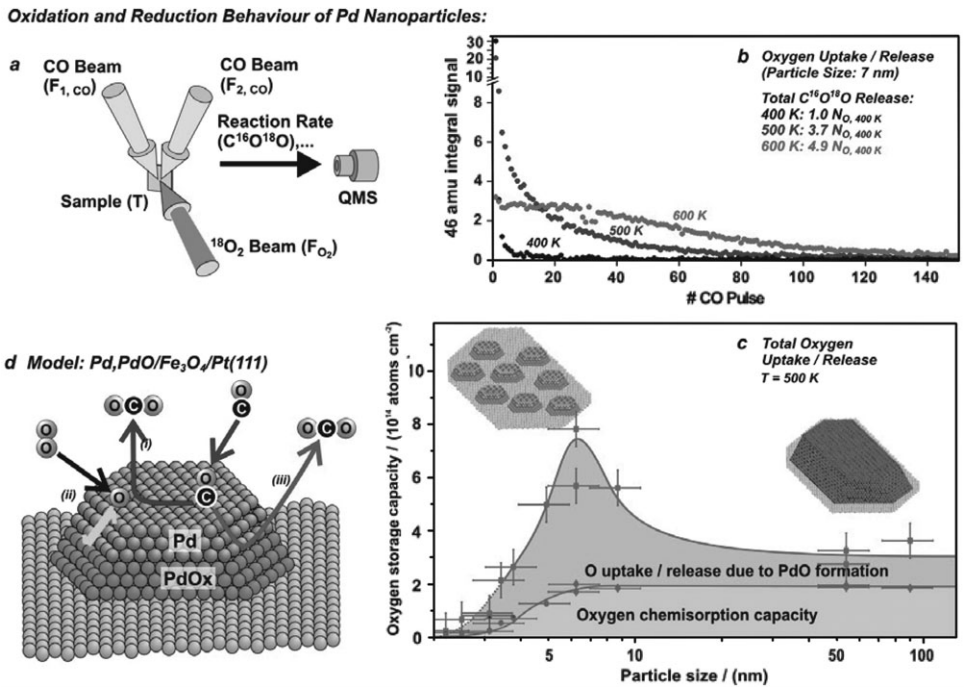

Fig. 11 Pulsed MB experiment probing the oxidation and reduction behaviour of Pd nanoparticles on Fe_3O_4/Pt(111). (a) The experimental setup involves the application of CO and $^{18}O_2$ pulse sequences. (b) CO_2 production providing information on the total amount of oxygen on the catalyst surface. Oxygen may be present in the form of chemisorbed oxygen or as a thin oxide layer at the Pd particle surface or interface. (c) Reversible oxygen uptake and release as a function of particle size. (d) Schematic model showing the different reaction channels during oxidation of CO on partially oxidized Pd particles (see text for details), from ref. 52 and 53.

by CO pulses to titrate the oxygen on the surface. At 400 K only chemisorbed oxygen was formed, showing a high reaction probability. As a result, the total CO_2 yield was relatively small, but the initial reaction rate was high. With increasing temperature the situation changed drastically. The initial reaction rate decreased, whereas the CO_2 production rate remained at a low but finite level for a very large number of CO pulses. The total CO_2 production by far exceeded the oxygen chemisorption capacity of the sample. Thus, the oxygen uptake and release is attributed to formation and decomposition of Pd oxide. It is apparent that the reaction probability for CO on PdO is significantly lower than for chemisorbed O on Pd particles.

We also investigated the formation and reactivity of the PdO phases on the Pd particles in great detail by means of PES, IRAS, and PSMB experiments.[41,52–54,74,134–136] The results could be summarized as follows: first of all, metallic and oxidized Pd areas were found to coexist over a relatively large temperature range. By means of PES (using synchrotron radiation, BESSY II) it was shown that the formation of PdO initially occurs at the Pd/Fe_3O_4 interface, before there is formation of surface PdO.[53] The latter result indicates that PdO is stabilized by interaction with the ionic support.

In a series of PSMB experiment the kinetics of PdO formation and decomposition was studied.[54] It was shown that, in addition to the conventional Langmuir–Hinshelwood pathway, two more steps are relevant for CO oxidation on partially oxidized particles (see Fig. 11d). First, there is incorporation of oxygen into and release of oxygen from the PdO phase onto the Pd metal. Thus, the PdO acts as an oxygen reservoir in oxidation reactions.[53] Secondly, there are indications for a direct reaction of chemisorbed CO with PdO. This type of direct reaction may, for example, occur at specific Pd/PdO interface sites. By means of well designed PSMB experiments the rates for all processes involved were recently individually determined. On the basis of these experimental results, we developed a microkinetic model for CO oxidation on partially oxidized Pd particles, taking explicitly into account PdO formation, decomposition and reaction of CO at active PdO sites.

With respect to the interpretation of particle size effects in catalysis, the size dependence of the oxidation behavior may play a critical role. Reversible oxygen uptake and release as a function of particle size were studied by means of a PSMB experiments. The nominal oxygen uptake per catalyst surface area showed a pronounced maximum as a function of particle size and metal loading (see Fig. 11c).[52] The reason is that intermediate-size particles (5–7 nm) are efficiently oxidized and reduced, whereas larger particles show strong kinetic hindrance to oxidation. In contrast, for smaller particles, oxidation is facile but small metal loading limits the oxygen uptake. In addition, there are experimental indications that full reduction of very small particles is hindered due to strong stabilization of the oxide by the support.[74]

Finally, we addressed the effect of Pd oxide formation on the catalytic activity. Towards this end, we first discuss the effect of formation of PdO on CO oxidation under steady-state conditions, before we will shift our attention to the influence of Pd oxidation on the oxidation and decomposition of methanol in the next section.

The effect of PdO formation on the catalytic CO oxidation was studied systematically by means of MB experiments.[41] Here we have to differentiate between two cases. At low temperature, the fraction of Pd particles covered by PdO is frozen. As a result of the lower reaction probability on PdO, the activity decreased monotonously with increasing the degree of pre-oxidation. At higher reaction temperature, the situation was substantially more complex as the degree of particle oxidation dynamically changed with the reaction conditions. As a result, slow hysteresis effect appeared upon changing from oxygen-rich to CO-rich conditions and back. This type of dynamic response of the catalyst surface to the ambient conditions has to be included in kinetic models in addition to the complex reaction mechanism discussed above.

Partially oxidized Pd nanoparticles supported on Al_2O_3 were also examined under mbar pressure conditions.[99,100] Such particles may form during CH_3OH oxidation and the results will be discussed in the following section. Nevertheless, at this point one should note that the spectroscopic results indicated a coexistence of metallic and oxidic surface areas supporting the structure model suggested here. The activity of various Pd–O species for CO oxidation, including oxidized Pd single crystals, thin films and nanoparticles, is compared in ref. 42. In summary, PdO_x species formed on the particles were found less active for CO oxidation than chemisorbed oxygen on metallic Pd.

9. Methanol oxidation and support effects

In the preceding section we showed that the oxidation of Pd particles is closely related to the size of the particles and their interaction with the support. Furthermore, we related Pd oxidation to the catalytic activity for CO oxidation. In this section, we will go one step further, and make an attempt to identify the role of the support and of Pd oxidation on the reactions of methanol.

In a first step, the interaction of methanol with Al_2O_3 supported Pd particles ($Pd/Al_2O_3/NiAl(110)$) was investigated. Two molecular adsorption states on the alumina support were identified, both of which were, however, characterized by a weak interaction.[35] Surface diffusion of molecularly bound methanol to the Pd particles is facile, even at low temperatures, and leads to an increased adsorption rate on the Pd particles due to the capture zone effect.[34] On the Pd particles, methanol decomposition *via* an initial scission of the O–H bond and methoxide formation turned out to compete with molecular desorption. The reaction probability for decomposition was found to depend sensitively on the presence of coadsorbates such as CO or atomic oxygen.[35] Detailed studies on both the mechanism and the kinetics of methanol decomposition have recently been published (ref. 34, 35, 55, 94 and 97, see also ref. 11).

In order to obtain information on the role of the support, we considered the interaction of methanol with $Fe_3O_4/Pt(111)$ and $Pd/Fe_3O_4/Pt(111)$.[137] Selected results are displayed in Fig. 12. The corresponding IR spectra for the Pd-free Fe_3O_4 support are shown in Fig. 12a. Both, weakly bound molecular

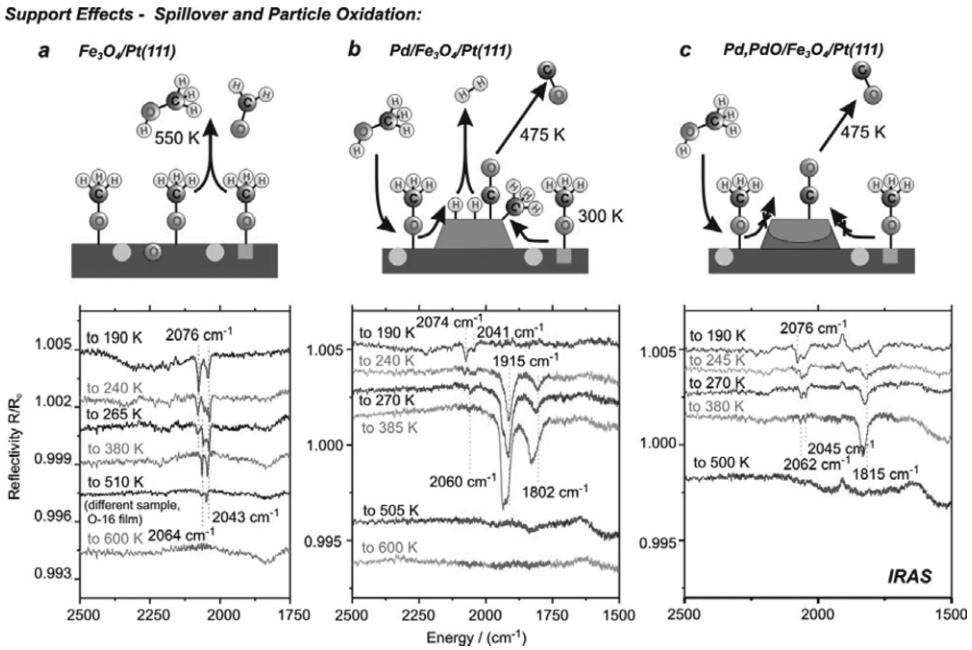

Fig. 12 IR reflection absorption spectra for the reaction of CH_3OH on (a) Fe_3O_4/Pt(111), (b) Pd/Fe_3O_4/Pt(111), and (c) Pd,PdO/Fe_3O_4/Pt(111). The methoxide species are present on the support, but show different thermal stability on the three systems. The differences indicate a strong influence of spillover from the support to the Pd particles, which depends on the oxidation state of the particles (see text for discussion), from ref. 137.

CD_3OD ($\nu_s(CD_3)$ = 2076 cm^{-1}, desorbing below 300 K) and the more strongly bound species, were identified (2064 cm^{-1}, 2043 cm^{-1}). On the basis of a comparison with previous studies, the latter may be tentatively assigned to stable methoxide moieties on the support (compare with ref. 35). It is noteworthy that the stability of these species on the Fe_3O_4 support is strongly enhanced as compared to the Al_2O_3/NiAl(110) case. Thermal decomposition occurred in a broad temperature range from 300 up to 600 K. In contrast to the alumina, for which only molecular desorption was found, different decomposition products were observed, such as CO and CH_2O.

Suprisingly, when a similar experiment was performed on partially Pd covered Fe_3O_4 support (Fig. 11b), the stability of methoxide was found strongly reduced as compared to the clean support. A possible interpretation involves the surface mobility of the intermediate and spillover of methoxide from the Fe_3O_4 to the Pd particles. As soon as the methoxide reaches the Pd particle at temperatures above 200 K, complete dehydrogenation to CO occurs (competing with the slow CO bond scission as discussed in section 5).

Finally, we investigated the influence of surface and interface oxidation on CH_3OH decomposition (see Fig. 11c). We found that the formation of interface oxide enhances the stability of the methoxy species. This finding is in line with the previous interpretation that spillover of methoxide species to the Pd particles and their subsequent decomposition are inhibited by the presence of the interface oxide at the particle boundary.

One expects that the strong dependence of the thermal stability of CH_3O species on the type of the support and, in particular, on the oxidation state of the Pd particles has a large influence on both the activity and selectivity. Indeed, first experiments indicated that the selectivity towards C–O *versus* the C–H bond scission strongly depends on the support material (at a similar Pd particle size, shape and density). Further experimental work is currently performed to verify these support and oxidation dependent effects.

Under ambient conditions, Pd nanoparticles (mean diameter 6 nm) on Al_2O_3/NiAl(110) were exposed to various CH_3OH/O_2 mixtures[99,100] (*e.g.* 15 mbar CH_3OH, 15 mbar O_2, filled up to 1 bar with He; temperature up to 500 K) (Fig. 13). A minimum temperature of 400 K was required for the reaction to occur (with CH_2O, CO_2 and H_2O detected as products by GC) because at lower temperature the particles were poisoned by CH_x (Fig. 13b). Whereas *via* SFG spectroscopy only bands were detected which are characteristic of CO adsorption on metallic Pd (Fig. 13a; such as bridge and on-top bonded CO; for an explanation of adsorption sites, SFG lineshapes and peak positions we refer to ref. 60), post-reaction XPS indicated that the Pd nanoparticles became partially oxidized during the reaction (Fig. 13c). The ~0.6 eV binding energy shift observed by XPS indicates an oxidation state in-between Pd and PdO (the binding energy shift for PdO would be 1.5 eV[138]). Using XPS and CO as a probe molecule showed that about 50% of the particle surface were oxidized, supporting the structure model suggested above. Nevertheless, when the Pd particles were fully oxidized before the reaction, no activity was observed anymore. Similar to CO oxidation, the PdO_x species were found less active for methanol oxidation than for metallic Pd.

Fig. 13d shows PM-IRAS spectra of CH_3OH decomposition and oxidation on a Pd(111) single crystal.[16] In the absence of oxygen the surface was covered by CO (~1840 cm^{-1}),

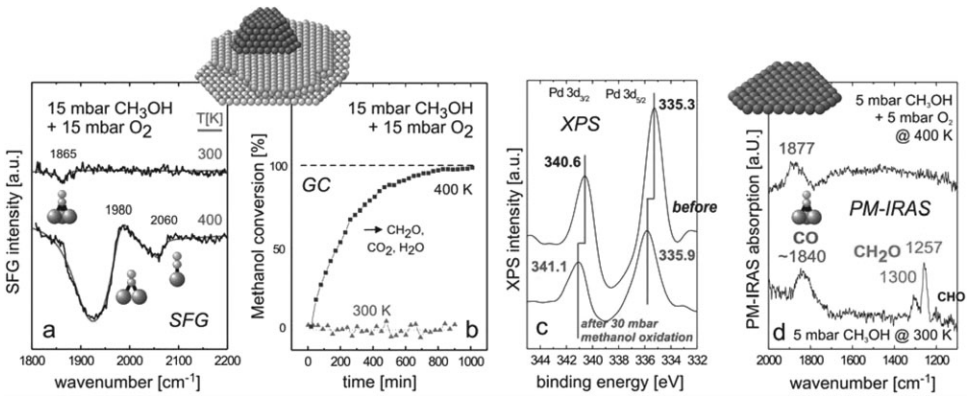

Fig. 13 SFG, XPS and PM-IRAS measurements during CH_3OH oxidation on Al_2O_3 supported Pd nanoparticles and on Pd(111), from ref. 16, 99 and 100.

CH_2O (1257 and 1300 cm^{-1}), CHO ($\sim$1200 cm^{-1}) and CH_x (the latter monitored by XPS) but no reaction products were observed by GC. In contrast, in the presence of oxygen at 400 K GC and PM-IRAS indicated formation of CH_2O, CO_2 and H_2O.[16] CO was the only surface species detected under reactive conditions (Fig. 13d) indicating rapid CH_3OH dehydrogenation *via* CH_2O to CO, followed by CO oxidation. The difference between the CO adsorption bands on Pd particles and Pd(111) is due to the different adsorption configurations on the model catalysts; for a detailed discussion we refer to ref. 16, 58 and 60. Note that, in contrast to the Pd particles, Pd(111) remained metallic during the reaction, again illustrating the difference between single crystals and supported nanoparticles.

SFG spectroscopy experiments were also carried out on Pd–Fe_3O_4/Pt(111) model catalysts[139] and the initial results are shown in Fig. 14. For relatively large Pd nanoparticles (*ca.* 10 nm) the CO spectra were characteristic, as expected, of adsorption on well-developed (111) facets.[56] The Pd–Fe_3O_4 model catalysts were thermally stable up to 600 K with hardly any changes detected by SFG (Fig. 14) or TPD.[139] These experiments demonstrated that Fe_3O_4 supported model catalysts are suitable for SFG spectroscopy, allowing one to study their interaction with methanol at high temperature.

10. Summary and outlook

In this review, we summarized the results of an integrated project which aimed at bridging surface science and heterogeneous catalysis, using reactions of methanol on Pd based catalysts as an example. A broad variety of catalytically active surfaces were studied, ranging from Pd single crystals over Pd nanoparticles supported on well-defined single crystal based oxide surfaces to particles supported on powder supports. In addition, bimetallic PdCo systems have been considered.

Studies were performed by a broad range of methods including many surface science techniques. A special focus was on the application of experimental methods, which allow one to bridge the pressure gap by performing spectroscopic and kinetic measurements from UHV to ambient conditions. Among these methods were vibrational spectroscopies such as IRAS, TR-IRAS, PM-IRAS, SFG, and DRIFTS in combination with MB methods and reactor studies.

In the low pressure region, detailed kinetic studies were performed by combining MB methods with time-resolved spectroscopy under reaction conditions. Based on these results, it was possible to develop detailed microkinetic models of methanol decomposition and oxidation, specifically taking into account multiple kinetic effects on complex catalyst surfaces such as the presence of different active sites. It was shown that the selectivity towards C–O *versus* C–H bond scission depends on the presence of special particle sites, leading to characteristic structure dependent effects. In particular, we focused on the influence of carbon and oxygen on activity and selectivity. Concerning the role of oxygen, detailed

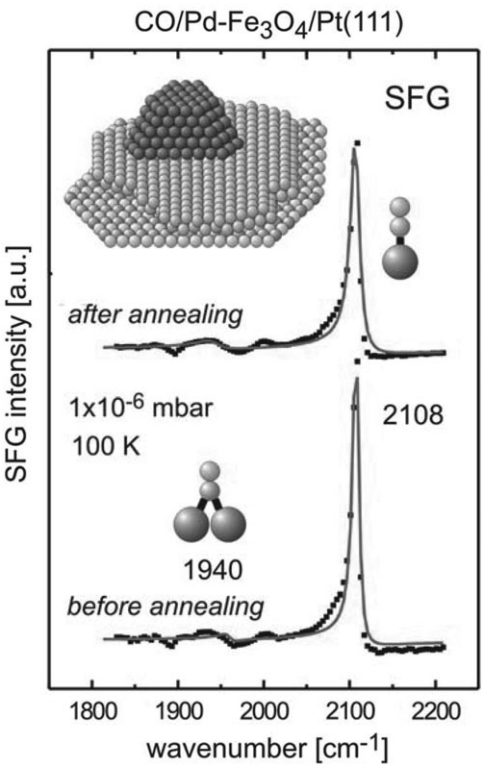

Fig. 14 SFG spectra of CO adsorption on Pd particles supported on Fe_3O_4 (100 K), before (lower trace) and after (upper trace) annealing in 1×10^{-6} mbar CO to 600 K, illustrating the thermal stability of the model system, from ref. 139.

mechanisms and models for oxide formation on the Pd particles were developed, including the pronounced size dependencies of these phenomena. Finally, support effects were studied, showing that the stability of intermediates on the support may have a major influence on the selectivity.

Combining SFG, PM-IRAS and GC allowed us to study the interaction of methanol and oxygen with supported Pd nanoparticles and Pd(111) at mbar pressure. The adsorption and reaction properties of Pd nanoparticles often differed from those of single crystal surfaces, *e.g.* Pd particles were more easily oxidized and also the C–O bond scission seems facilitated for nanoparticles. The reaction routes that are of minor importance under UHV may gain substantial influence at mbar pressures. We also demonstrated the suitability of the new Pd–Fe_3O_4/Pt(111) model catalysts for SFG spectroscopy.

Pd particles were shown to catalyze methanol decomposition under continuous flow conditions. In accordance with the fast C–H dissociation pathway, CO was found to be the main product at temperatures well above 150 °C. At and below 150 °C only insignificant amounts of CO were detected in the gas phase although adsorbed CO was observed on the surface by IR spectroscopy. Based on experiments with Pd particles under UHV conditions, this behavior was rationalized by desorption-limited kinetics. Apart from Pd particles, also bimetallic CoPd particles were studied in a twofold approach, *i.e.* under ambient and UHV conditions. In both cases the same result was obtained, namely the activity of the pure Pd particles was somewhat higher as compared to the bimetallic particles for which the CO yield was almost independent of the bimetallic composition.

As a significant achievement of these concerted experimental and theoretical efforts, a fruitful modelling strategy was developed that affords a realistic theoretical description of supported nanoparticles with $\geq 10^3$ metal atoms, which are experimentally explored as model catalysts. This novel approach employs ordered 3-D nanoparticles with structures cut from bulk metal and terminated by low-index surfaces. Most importantly, such models were successfully applied to quantify the reaction and activation energies of CH_3O decomposition to CH_3 and O without any local symmetry constraint imposed on reactants, products and transition state species. Beyond assisting in the spectroscopic characterization of surface sites on Pd nanoparticles, the theoretical activities lead to a considerably deeper understanding of how atomic carbon deposits are formed on supported Pd species and how they affect the reactivity of the latter.

In summary, the results of the reviewed joint project show that, by combining suitable experimental and theoretical approaches, a detailed picture of a complex catalytic reaction system can be developed, which provides a microscopic-level understanding of structure, size and support dependent effects in heterogeneous catalysis, ranging from ideal ultra-high vacuum to real ambient pressure conditions.

Acknowledgements

The work presented in this review was performed from 2000 to 2006 within the joint project "Methanol Synthesis and Partial Oxidation on Well-Defined Supported Model Catalysts" within the DFG Priority Program 1091 "Bridging the Pressure Gap between Ideal and Real Systems in Heterogeneous Catalysis".

J. L. (Project Part A) would like to thank B. Brandt, J. Hartmann, J. Hoffmann, V. Johanek, M. Laurin, T. Schalow and S. Schauermann, who showed great enthusiasm performing MB experiments and microkinetic simulations. We are also grateful to H. Kuhlenbeck, S. Guimond and the BESSY staff for help while performing PES experiments at BESSY (Berlin), Sh. K. Shaikhutdinov, D. E. Starr and M. Heemeier for performing STM measurements, and A. Grant and B. Kasemo for providing samples prepared by electron beam lithography, V. Zhdanov for the introduction to MC simulation and C. R. Henry for cooperation and many helpful discussions.

G.R. (Project Part B) is very grateful to T. Dellwig, H. Unterhalt, L. Hu, P. Galletto, M. Morkel, O. Rodriguez de la Fuente, M. Borasio, F. Höbel, B. Kell, J. Silvestre-Albero, and A. Bandara, who all contributed to the results presented. Collaborations with V. I. Bukhtiyarov (Boreskov Institute of Catalysis; HP-XPS), K. Hayek (Universität Innsbruck, HRTEM), and T. Klüner (Universität Oldenburg; DFT) are gratefully acknowledged.

K.M.N. and N.R. (Project Part C) are grateful to C. Inntam, K. H. Lim, R. Sahnoun and I. V. Yudanov for their invaluable contributions to the success of the theoretical part of the project. N.R. and J.L. acknowledge support by the Fonds der Chemischen Industrie (Germany).

M.B. (Project Part D) is indebted to the following coworkers who contributed significantly to the work discussed here: H. Borchert, B. Jürgens, T. Nowitzki and V. Zielasek. Very fruitful and enjoyable collaborations with C. R. Henry and S. Giorgio (CNRS Marseille: preparation of the Pd and bimetallic PdCo particles on MgO and their TEM characterization) and T. Risse (FHI, Berlin: IR spectroscopy and FMR measurements on the UHV model systems) are gratefully acknowledged.

References

1 *Handbook of Heterogeneous Catalysis*, ed. G. Ertl, H. Knözinger and J. Weitkamp, VCH, Weinheim, 1997.
2 J. M. Thomas and W. J. Thomas, *Principle and Practice of Heterogeneous Catalysis*, VCH, Weinheim, 1997.
3 D. W. Goodman, *J. Catal.*, 2003, **216**, 213.
4 H.-J. Freund, *Catal. Today*, 2005, **100**, 3.
5 D. W. Goodman, *Surf. Rev. Lett.*, 1995, **2**, 9.
6 G. Ertl, *Adv. Catal.*, 2000, **45**, 1.
7 H.-J. Freund, M. Bäumer and H. Kuhlenbeck, *Adv. Catal.*, 2000, **45**, 333.
8 C. R. Henry, *Surf. Sci. Rep.*, 1998, **31**, 231.
9 V. P. Zhdanov and B. Kasemo, *Surf. Sci. Rep.*, 2000, **39**, 25.
10 K. Hayek, M. Fuchs, B. Klötzer, W. Reichl and G. Rupprechter, *Top. Catal.*, 2000, **13**, 55.
11 J. Libuda and H.-J. Freund, *Surf. Sci. Rep.*, 2005, **57**, 157.
12 C. C. Chusuei, X. Lai, K. Luo and D. W. Goodman, *Top. Catal.*, 2001, **14**, 71.
13 G. A. Somorjai and G. Rupprecher, *J. Phys. Chem. B*, 1999, **103**, 1623.
14 T. Dellwig, G. Rupprechter, H. Unterhalt and H.-J. Freund, *Phys. Rev. Lett.*, 2000, **85**, 776.
15 G. Rupprechter, *Adv. Catal.*, 2007, **51**, 133.
16 M. Borasio, O. R. d. l. Fuente, G. Rupprechter and H.-J. Freund, *J. Phys. Chem. B*, 2005, **109**, 17791.

17 C. Hess, E. Ozensoy and D. W. Goodman, *J. Phys. Chem. B*, 2003, **107**, 2759.
18 H. Topsoe, *J. Catal.*, 2003, **216**, 155.
19 S. Giorgio, S. S. Joao, S. Nitsche, D. Chaudanson, G. Sitja and C. R. Henry, *Ultramicroscopy*, 2006, **106**, 503.
20 B. L. M. Hendriksen, S. C. Bobaru and J. W. M. Frenken, *Top. Catal.*, 2005, **36**, 43.
21 V. V. Kaichev, I. P. Prosvirin, V. I. Bukhtiyarov, H. Unterhalt, G. Rupprechter and H.-J. Freund, *J. Phys. Chem. B*, 2003, **107**, 3522.
22 D. Teschner, A. Pestryakov, E. Kleimenkov, M. Havecker, H. Bluhm, H. Sauer, A. Knop-Gericke and R. Schlögl, *J. Catal.*, 2005, **230**, 186.
23 J. Pantförder, S. Pollmann, J. F. Zhu, B. D. R. Denecke and H.-P. Steinrück, *Rev. Sci. Instrum.*, 2005, **76**, 14102.
24 M. Rössler, P. Geng and J. Wintterlin, *Rev. Sci. Instrum.*, 2005, **76**, 23705.
25 I. Wender, *Fuel Process. Technol.*, 1996, **48**, 189.
26 X. M. Liu, G. Q. Lu, Z. F. Yan and B. J. Yan, *Ind. Eng. Chem. Res.*, 2003, **42**, 6518.
27 G. W. Huber, S. Iborra and A. Corma, *Chem. Rev.*, 2006, **106**, 4044.
28 R. J. Farrauto and C. Bartholomew, *Introduction to Industrial Catalytic Processes*, Chapmann & Hall, London, 1997.
29 M. L. Poutsma, L. F. Elek, P. A. Ibarbia, A. P. Risch and J. A. Rabo, *J. Catal.*, 1978, **52**, 157.
30 J. P. Hindermann, G. J. Hutchings and A. Kiennemann, *Catal. Rev. Sci. Eng.*, 1993, **35**, 1.
31 E. M. Cordi and J. L. Falconer, *J. Catal.*, 1996, **162**, 104.
32 M. L. Cubeiro and J. L. G. Fierro, *J. Catal.*, 1998, **179**, 150.
33 R. Shiozaki, T. Hayakawa, Y. Y. Liu, T. Ishii, M. Kumagai, S. Hamakawa, K. Suzuki, T. Itoh, T. Shishido and K. Takehira, *Catal. Lett.*, 1999, **58**, 131.
34 J. Hoffmann, S. Schauermann, V. Johánek, J. Hartmann and J. Libuda, *J. Catal.*, 2003, **213**, 176.
35 S. Schauermann, J. Hoffmann, V. Johánek, J. Hartmann and J. Libuda, *Phys. Chem. Chem. Phys.*, 2002, **4**, 3909.
36 F. Zaera, *Chem. Rec.*, 2005, **5**, 133.
37 E. Lundgren, G. Kresse, C. Klein, M. Borg, J. N. Andersen, M. De Santis, Y. Gauthier, C. Konvicka, M. Schmid and P. Varga, *Phys. Rev. Lett.*, 2002, **88**, 246103.
38 M. Todorova, E. Lundgren, V. Blum, A. Mikkelsen, S. Gray, J. Gustafson, M. Borg, J. Rogal, K. Reuter, J. N. Andersen and M. Scheffler, *Surf. Sci.*, 2003, **541**, 101.
39 G. Zheng and E. I. Altmann, *J. Phys. Chem. B*, 2002, **2002**, 1048.
40 B. L. M. Hendriksen, S. C. Bobaru and J. W. M. Frenken, *Surf. Sci.*, 2004, **552**, 229.
41 T. Schalow, B. Brandt, M. Laurin, S. Schauermann, J. Libuda and H.-J. Freund, *J. Catal.*, 2006, **242**, 58.
42 H. Gabasch, A. Knop-Gericke, R. Schlögl, M. Borasio, C. Weilach, G. Rupprechter, S. Penner, B. Jenewein, K. Hayek and B. Klötzer, *Phys. Chem. Chem. Phys.*, 2007, **9**, 533.
43 G. Rupprechter, T. Dellwig, H. Unterhalt and H.-J. Freund, *Top. Catal.*, 2001, **15**, 19.
44 H. Unterhalt, G. Rupprechter and H.-J. Freund, *J. Phys. Chem. B*, 2002, **106**, 356.
45 O. Rodriguez de la Fuente, M. Borasio, P. Galetto, G. Rupprechter and H.-J. Freund, *Surf. Sci.*, 2004, **566–568**, 740.
46 T. W. Hansen, J. B. Wagner, P. L. Hansen, S. Dahl, H. Topsoe and C. J. H. Jacobsen, *Science*, 2001, **294**, 1508.
47 J. Libuda, I. Meusel, J. Hartmann and H.-J. Freund, *Rev. Sci. Instrum.*, 2000, **71**, 4395.
48 M. P. D'Evelyn and R. J. Madix, *Surf. Sci. Rep.*, 1984, **3**, 413.
49 G. Scoles, *Atomic and Molecular Beam Methods*, Oxford University Press, Oxford, 1988.
50 C. T. Rettner, D. J. Auerbach, J. C. Tully and A. W. Kleyn, *J. Phys. Chem.*, 1996, **100**, 13021.
51 A. W. Kleyn, *Chem.Soc. Rev.*, 2003, **32**, 87.
52 T. Schalow, B. Brandt, D. E. Starr, M. Laurin, S. K. Shaikhutdinov, S. Schauermann, J. Libuda and H.-J. Freund, *Angew. Chem., Int. Ed.*, 2006, **45**, 3775.
53 T. Schalow, M. Laurin, B. Brandt, S. Schauermann, S. Guimond, H. Kuhlenbeck, D. E. Starr, S. k. Shaikhutdinov, J. Libuda and H.-J. Freund, *Angew. Chem., Int. Ed.*, 2005, **44**, 7601.
54 B. Brandt, T. Schalow, M. Laurin, S. Schauermann, J. Libuda and H.-J. Freund, *J. Phys. Chem. B*, in press.
55 S. Schauermann, J. Hoffmann, V. Johánek, J. Hartmann, J. Libuda and H.-J. Freund, *Angew. Chem., Int. Ed.*, 2002, **41**, 2532.
56 G. Rupprechter, H. Unterhalt, M. Morkel, P. Galletto, L. Hu and H.-J. Freund, *Surf. Sci.*, 2002, **502–503**, 109.
57 G. Rupprechter, M. Morkel, H.-J. Freund and R. Hirschl, *Surf. Sci.*, 2004, **554**, 43.
58 M. Morkel, G. Rupprechter and H.-J. Freund, *Surf. Sci. Lett.*, 2005, **588**, L209.
59 F. Höbel, A. Bandara, G. Rupprechter and H.-J. Freund, *Surf. Sci.*, 2006, **600**, 963.
60 M. Morkel, H. Unterhalt, T. Klüner, G. Rupprechter and H.-J. Freund, *Surf. Sci.*, 2005, **586**, 146.
61 J. Hoffmann, S. Schauermann, J. Hartmann, V. P. Zhdanov, B. Kasemo, J. Libuda and H.-J. Freund, *Chem. Phys. Lett.*, 2002, **354**, 403.
62 J. Hoffmann, I. Meusel, J. Hartmann, J. Libuda and H.-J. Freund, *J. Catal.*, 2001, **204**, 378.
63 M. Laurin, V. Johanek, A. W. Grant, B. Kasemo, J. Libuda and H.-J. Freund, *J. Chem. Phys.*, 2005, **123**, 054701.
64 M. Laurin, V. Johanek, A. W. Grant, B. Kasemo, J. Libuda and H.-J. Freund, *J. Chem. Phys.*, 2005, **122**, 084713.
65 V. Johánek, M. Laurin, A. W. Grant, B. Kasemo, C. R. Henry and J. Libuda, *Science*, 2004, **304**, 5677.
66 H.-J. Freund, M. Bäumer, J. Libuda, T. Risse, G. Rupprechter and S. Shaikhutdinov, *J. Catal.*, 2003, **216**, 223.
67 J. Libuda, F. Winkelmann, M. Bäumer, H.-J. Freund, T. Bertrams, H. Neddermeyer and K. Müller, *Surf. Sci.*, 1994, **318**, 61.
68 G. Kresse, M. Schmid, E. Napetschnig, M. Shishkin, L. Kohler and P. Varga, *Science*, 2005, **308**, 1440.
69 W. Weiss and W. Ranke, *Prog. Surf. Sci.*, 2002, **70**, 1.
70 C. Lemire, R. Meyer, V. Henrich, S. K. Shaikhutdinov and H.-J. Freund, *Surf. Sci.*, 2004, **572**, 103.
71 R. Meyer, S. K. Shaikhutdinov and H.-J. Freund, *Z. Phys. Chem.*, 2004, **218**, 905.
72 M. Bäumer, J. Biener and R. J. Madix, *Surf. Sci.*, 1999, **432**, 189.
73 I. Meusel, J. Hoffmann, J. Hartmann, J. Libuda and H.-J. Freund, *J. Phys. Chem. B*, 2001, **105**, 3567.
74 T. Schalow, B. Brandt, D. E. Starr, M. Laurin, S. K. Shaikhutdinov, S. Schauermann, J. Libuda and H.-J. Freund, *Phys. Chem. Chem. Phys.*, 2007, 1347–1361.
75 J. Silvestre-Albero, G. Rupprechter and H.-J. Freund, *J. Catal.*, 2006, **240**, 58.
76 G. Rupprechter, V. V. Kaichev, H. Unterhalt, M. Morkel and V. I. Bukhtiyarov, *Appl. Surf. Sci.*, 2004, **235**, 26.
77 M. Morkel, G. Rupprechter and H.-J. Freund, *J. Chem. Phys.*, 2003, **119**, 10853.
78 M. Morkel, H. Unterhalt, M. Salmeron, G. Rupprecher and H.-J. Freund, *Surf. Sci.*, 2003, **532–535**, 103.
79 V. Johanek, M. Laurin, J. Hoffmann, S. Schauermann, A. W. Grant, B. Kasemo, J. Libuda and H.-J. Freund, *Surf. Sci. Lett.*, 2004, **561**, L218.
80 M. Heemeier, A. F. Carlsson, N. Naschitzki, M. Schmal, M. Bäumer and H.-J. Freund, *Angew. Chem., Int. Ed.*, 2002, **41**, 4073.
81 A. Carlsson, N. Naschitzki, M. Bäumer and H.-J. Freund, *J. Phys. Chem. B*, 2003, **107**, 778.
82 H. Borchert, B. Jürgens, V. Zielasek, G. Rupprechter, S. Giorgio, C. R. Henry and M. Bäumer, *J. Catal.*, 2007, **247**, 145.
83 H. Borchert, B. Jürgens, T. Nowitzki, V. Zielasek, S. Giorgio, C. R. Henry and M. Bäumer, in preparation.
84 I. V. Yudanov, R. Sahnoun, K. M. Neyman and N. Rösch, *J. Chem. Phys.*, 2002, **117**, 9887.
85 M. Bäumer and H.-J. Freund, *Prog. Surf. Sci.*, 1999, **61**, 127.
86 N. Rösch, V. A. Nasluzov, K. M. Neyman, G. Pacchioni and G. N. Vayssilov, in *Computational Material Science*, ed. J. Leszczynski, Elsevier, Amsterdam, 2004, p. 365.
87 K. M. Neyman and F. Illas, *Catal. Today*, 2005, **105**, 2.
88 B. I. Dunlap and N. Rösch, *Adv. Quantum Chem.*, 1990, **21**, 317.
89 T. Belling, T. Grauschopf, S. Krüger, M. Mayer, F. Nörtemann, M. Staufer and C. Zenger and N. Rösch, in *High Performance Scientific and Engineering Computing*, eds. H.-J. Bungartz, F. Durst and C. Zenger, Springer, Heidelberg, 1999, p. 439.
90 T. Belling, T. Grauschopf, S. Krüger, F. Nörtemann, M. Staufer, M. Mayer, V. A. Nasluzov, U. Birkenheuer, A. Hu, A. V. Matveev, A. M. Shor, M. S. K. Fuchs-Rohr, K. M. Neyman, D. I. Ganyushin, T. Kerdcharoen, A. Woiterski, A. B. Gordienko, S. Majumder

and N. Rösch, *ParaGauss, Version 3.0*, Technische Universität München, Munich, 2004.
91 S. Krüger, S. Vent and N. Rösch, *Ber. Bunsen-Ges. Phys. Chem.*, 1997, **101**, 1640.
92 G. Pacchioni, S. Krüger and N. Rösch, in *Metal Clusters in Chemistry*, ed. P. Braunstein, L. A. Oro and P. R. Raithby, Wiley-VCH, Weinheim, 1999, p. 1392.
93 I. V. Yudanov, K. M. Neyman and N. Rösch, *Phys. Chem. Chem. Phys.*, 2006, **8**, 2396.
94 S. Schauermann, J. Hoffmann, V. Johánek, J. Hartmann, J. Libuda and H.-J. Freund, *Catal. Lett.*, 2002, **84**, 209.
95 I. V. Yudanov, R. Sahnoun, K. M. Neyman, N. Rösch, J. Hoffmann, S. Schauermann, V. Johánek, H. Unterhalt, G. Rupprechter, J. Libuda and H.-J. Freund, *J. Phys. Chem. B*, 2003, **107**, 255.
96 S. Bertarione, D. Scarano, A. Zecchina, V. Johanek, J. Hoffmann, S. Schauermann, M. M. Frank, J. Libuda, G. Rupprechter and H.-J. Freund, *J. Phys. Chem. B*, 2004, **108**, 3603.
97 J. Libuda, *ChemPhysChem*, 2004, **5**, 625.
98 S. Bertarione, D. Scarano, A. Zecchina, V. Johanek, J. Hoffmann, S. Schauermann, J. Libuda, G. Rupprechter and H.-J. Freund, *J. Catal.*, 2004, **223**, 64.
99 M. Borasio, Dissertation Thesis, Freie Universität Berlin, 2006.
100 G. Rupprechter, H. Unterhalt, M. Borasio, M. Morkel and H.-J. Freund, *Annu. Rep. Max Planck Soc. (Jahrbuch)*, 2005, 193.
101 K. Wolter, O. Seiferth, J. Libuda, H. Kuhlenbeck, M. Bäumer and H.-J. Freund, *Surf. Sci.*, 1998, **402–404**, 428.
102 J. Libuda and H.-J. Freund, *J. Phys. Chem. B*, 2002, **106**, 4901.
103 J. Libuda, *Surf. Sci.*, 2005, **587**, 55.
104 F. M. Hoffmann, *Surf. Sci. Rep.*, 1983, **3**, 107.
105 P. Hollins, *Surf. Sci. Rep.*, 1992, **16**, 51.
106 Z. X. Chen, K. M. Neyman, K. H. Lim and N. Rösch, *Langmuir*, 2004, **20**, 8086.
107 M. Morkel, V. V. Kaichev, G. Rupprechter, H.-J. Freund, I. P. Prosvirin and V. I. Bukhtiyarov, *J. Phys. Chem. B*, 2004, **108**, 12955.
108 K. M. Neyman, C. Inntam, A. B. Gordienko, I. V. Yudanov and N. Rösch, *J. Chem. Phys.*, 2005, **122**, 174705.
109 K. M. Neyman, G. N. Vayssilov and N. Rösch, *J. Organomet. Chem.*, 2004, **689**, 4384.
110 J. F. Goellner, K. M. Neyman, M. Mayer, F. Nörtemann, B. C. Gates and N. Rösch, *Langmuir*, 2000, **16**, 2736.
111 I. V. Yudanov, K. M. Neyman and N. Rösch, *Phys. Chem. Chem. Phys.*, 2004, **6**, 116.
112 K. H. Lim, K. M. Neyman and N. Rösch, *Chem. Phys. Lett.*, 2006, **432**, 184.
113 M. K. Rose, A. Borg, T. Mitsui, D. F. Ogletree and M. Salmeron, *J. Chem. Phys.*, 2001, **115**, 10927.
114 L. Guczi, Z. Schay, G. Stefler and F. Mizukami, *J. Mol. Catal. A: Chem.*, 1999, **141**, 177.
115 L. Guczi, L. Borko, Z. Schay, D. Bazin and F. Mizukami, *Catal. Today*, 2001, **65**, 51.
116 C. T. Campbell, *Annu. Rev. Phys. Chem.*, 1990, **41**, 775.
117 J. A. Rodriguez, *Surf. Sci. Rep.*, 1996, **24**, 223.
118 A. Carlsson, N. Naschitzki, M. Bäumer and H.-J. Freund, *J. Chem. Phys.*, 2003, **119**, 10885.
119 M. Frank and M. Bäumer, *Phys. Chem. Chem. Phys.*, 2000, **2**, 3723.
120 D. A. Chen and C. M. Friend, *J. Phys. Chem. B*, 1997, **101**, 5712.
121 H. Conrad, G. Ertl, J. Küppers and E. E. Latta, *Surf. Sci.*, 1977, **65**, 245.
122 R. Imbihl and J. E. Demuth, *Surf. Sci.*, 1986, **173**, 395.
123 S.-L. Chang and P. A. Thiel, *J. Chem. Phys.*, 1988, **88**, 2071.
124 X. Guo, A. Hoffman and J. T. Yates, Jr, *J. Chem. Phys.*, 1989, **90**, 5787.
125 V. A. Bondzie, P. Kleban and D. J. Dwyer, *Surf. Sci.*, 1996, **347**, 319.
126 E. H. Voogt, A. J. M. Mens and J. W. G. O. L. J. Gijzeman, *Surf. Sci.*, 1997, **373**, 210.
127 F. P. Leisenberger, G. Koller, M. Sock, S. Surnev, M. G. Ramsey, F. P. Netzer, B. Klötzer and K. Hayek, *Surf. Sci.*, 2000, **445**, 380.
128 V. A. Bondzie, P. H. Kleban and D. J. Dwyer, *Surf. Sci.*, 2000, **465**, 266.
129 G. Zheng and E. I. Altman, *Surf. Sci.*, 2000, **462**, 151.
130 G. Zheng and E. I. Altman, *Surf. Sci.*, 2002, **504**, 253.
131 E. Lundgren, J. Gustafson, A. Mikkelsen, J. N. Andersen, A. Stierle, H. Dosch, M. Todorova, J. Rogal, K. Reuter and M. Scheffler, *Phys. Rev. Lett.*, 2004, **92**, 046101.
132 M. Todorova, K. Reuter and M. Scheffler, *Phys. Rev. B*, 2005, **71**, 195403.
133 A. Stierle, N. Kasper, H. Dosch, E. Lundgren, J. Gustafson, A. Mikkelsen and J. N. Andersen, *J. Chem. Phys.*, 2005, **122**, 44706.
134 T. Schalow, B. Brandt, M. Laurin, S. Guimond, H. Kuhlenbeck, S. Schauermann, J. Libuda and H.-J. Freund, *Surf. Sci.*, 2006, **600**, 2528.
135 T. Schalow, B. Brandt, D. E. Starr, M. Laurin, S. Schauermann, S. K. Shaikhutdinov, J. Libuda and H.-J. Freund, *Catal. Lett.*, 2006, **107**, 189.
136 T. Schalow, B. Brandt, M. Laurin, S. Guimond, D. E. Starr, S. K. Shaikhutdinov, S. Schauermann, J. Libuda and H.-J. Freund, *Top. Catal.*, in press.
137 B. Brandt, T. Schalow, J. H. Fischer, S. Schauermann, J. Libuda and H.-J. Freund, unpublished.
138 O. Demoulin, G. Rupprechter, I. Seunier, B. L. Clef, M. Navez and P. Ruiz, *J. Phys. Chem. B*, 2005, **109**, 20454.
139 F. Höbel, Dissertation Thesis, Technische Universität Berlin, in preparation, 2007.
140 I. Meusel, J. Hoffmann, J. Hartmann, M. Heemeier, M. Bäumer, J. Libuda and H.-J. Freund, *Catal. Lett.*, 2001, **71**, 5.
141 D. E. Starr and S. K. Shaikhutdinov, unpublished.
142 M. Bäumer and M. Frank, unpublished.
143 Y. Liu, T. Hayakawa, T. Ishii, M. Kumagai, H. Yasuda, K. Suzuki, S. Hamakawa and K. Murata, *Appl. Catal., A*, 2001, **210**, 301.
144 N. Iwasa and N. Takezawa, *Top. Catal.*, 2003, **22**, 215.

